2D and 3D Multiphysics Voronoi Cells, Based on Radial Basis Functions, for Direct Mesoscale Numerical Simulation (DMNS) of the Switching Phenomena in Ferroelectric Polycrystalline Materials

Peter L. Bishay[1] **and Satya N. Atluri**[1]

Abstract: In this paper, 2D and 3D Multiphysics Voronoi Cells (MVCs) are developed, for the Direct Mesoscale Numerical Simulation (DMNS) of the switching phenomena in ferroelectric polycrystalline materials. These arbitrarily shaped MVCs (arbitrary polygons in 2D, and arbitrary polyhedrons in 3D with each face being an arbitrary polygon) are developed, based on assuming radial basis functions to represent the internal primal variables (mechanical displacements and electric potential), and assuming linear functions to represent the primal variables on the element boundaries. For the 3D case, the linear functions used to represent the primal variables on each of the polygonal surfaces of the polyhedral VCs are the Barycentric Washspress functions. The present 2D MVC is denoted as MVC-RBF, while the 3D MVC is denoted as MVC-RBF-W. Each MVC can represent a single grain or crystallite, with an irregular polygonal shape for the 2D case, and an irregular polyhedral shape for the 3D case. In this work, a nonlinear constitutive model is used to describe the evolution of volume fractions of the constitutive-variants in each grain, as the electric or mechanical loading changes. This constitutive model is based on satisfying a local dissipation inequality in each grain in the polycrystalline that yields the minimum Gibbs free energy in this grain. This requirement should always hold in order to be consistent with the second law of thermodynamics and is used to govern the switching process in each grain in each simulation step. Since the interaction between the grains during the loading cycles has a profound influence on the switching phenomena, it is important to simulate the grains with geometrical shapes that are similar to the real shapes of the grains as seen in the lab experiments. Hence the use of 3D MVCs, which allow for the presence of all the six variants of the constitutive relations, together with the randomly generated crystallographic axes in each grain (or MVC), as done in the present paper, is

---

[1] International Collaboratory for Fundamental Studies in Engineering Sciences, University of California, Irvine, CA, USA

considered to be the most realistic analytical model that can be used for the direct mesoscale numerical simulation of polycrystalline ferroelectric materials.

Keywords: Ferroelectric, ferroelastic, switching, Gibbs free energy, Voronoi cells, radial basis functions, Barycentric coordinates, collocation.

1   Introduction and literature review

Ferroelectric materials have a linear behavior, similar to piezoelectric materials, at very low values of applied mechanical and electrical loads. At high intensities of an applied electric field, for instance, the behavior of the material becomes non-linear, and both the hysteresis loop of the macroscopic polarization vs. electric field, and the butterfly loop of the macroscopic strain vs. electric field, appear. Piezoelectric materials have spontaneous polarization; ferroelectric materials have the ability to reorient their spontaneous polarization with the application of an external field. This macroscopic behavior is actually based on mechanisms that happen in smaller scales. A polycrystalline ferroelectric ceramic is composed of an aggregate of grains separated by grain-boundaries, in the mesoscale. Within a grain, all the unit cells have the same crystallographic axes. Each grain has a random shape and is subdivided into several domains. A domain is a region in the grain where all the unit cells composing it have the same orientation of their asymmetry or the same spontaneous polarization direction. Domains of a grain are separated by domain walls. The reorientation of spontaneous polarization in ferroelectric materials is principally controlled by the motion of domain walls. Polarization reorientation within one phase can be induced by either applied stress (ferroelastic switching) or electric field (ferroelectric switching). Ferroelectric polycrystalline material behavior is more complicated than single crystals as each of the randomly oriented grains is a constrained single crystal subjected to local stress and electric field due to grain boundaries and local inhomogeneities [Webber (2008)]. In a tetragonal unit cell, the polarization switching occurs when an applied electric field exceeds the coercive field (which is the magnitude of electric field at zero polarization intensity on the electric field-electric displacement hysteresis response) and thus moves the central ion from one of the six off-center tetragonal sites to another. This changes the polar direction to the one that is most closely aligned with the applied electric field. In a polycrystalline ceramic, a crystallite usually has six different types of constitutive variants that are combined to form a complicated domain structure/pattern. Therefore, switching process is much more complicated in a polycrystalline material than in a unit cell.

Modeling a ferroelectric polycrystalline using the finite element method has been performed during the past 15 years, using different constitutive models [Hwang

and McMeeking (1998, 1999); Steinkopff (1999); Kamlah *et al.* (2005); Arock-iarajan *et al.* (2006, 2007); Haug *et al.* (2007); Menzel *et al.* (2008); Pathak and McMeeking (2008) among others]. Finite element modeling can deal with complex boundary value problems and explicitly takes the interaction between neighboring grains (inter-granular effects) into account. Randomly oriented crystal axes within the elements, or rather grains, together with the corresponding material properties realize the locally anisotropic nature of the polycrystalline ferroelectric specimen. A macroscale finite element model for an electro-mechanically coupled material has been suggested by Ghandi and Hagwood (1996). The phase/polarization state of materials is represented by internal variables in each element, which are updated in each simulation step based on a phenomenological model. Mesoscale finite element models has been developed by [Hwang and McMeeking (1998, 1999); Huo and Jiang (1997, 1998)]. The former modeled each crystallite as a cubic element with only one type of variant, with the tetragonal orientation for each element selected randomly. When an element satisfies a given switching criterion, switching occurs in the element and the tetragonal axis changes to a different permitted direction immediately. The latter modeled a crystallite as a body of mixture consisting of distinct types of constitutive variants, and characterized a grain by the values of volume fractions of variants. The volume fractions are regarded as internal variables and updated at each simulation step by a switching criterion. Kim and Jiang (2002) modeled the rate-dependent behavior of ferroelectric ceramics. They considered each crystal grain as a regular hexagon which was modeled by 12 triangular elements. As in [Huo and Jiang (1997, 1998)], they regarded a finite element as a continuum body of mixture characterized by the volume fractions of the existing variants. Haug *et al.* (2007) also modeled each grain using triangular or hexagonal elements. Kamlah *et al.* (2005) modeled each crystal grain as a rectangular element.

Ferroelectric polycrystalline grains have random polyhedral shapes. Hence, to better model the polycrystalline microstructure, Voronoi Cells which are based on Dirichlet tessellation of the considered body into irregular polygons in 2D, or irregular polyhedra in 3D, should be used. In this way, a grain in a representative ferroelectric microstructure is surrounded by a varying number of differently shaped neighboring grains. This can also increase the computational efficiency since each grain is modeled by a single Voronoi Cell and no further sub-discretization is required in one crystal grain structure. In consequence, Voronoi-based discretizations, together with randomly generated crystallographic axes for each grain, in general, represent the overall polycrystalline microstructure better. It is important to note that using regular elements (quadrilaterals in 2D or bricks in 3D) to model ferroelectric materials gives the same macroscopic response as that of the irregular

Voronoi-cell elements. However, the local distributions of stress, strain, electric field and electric displacement are different. This was shown in [Jayabal *et al.* (2011)] for the 2D case, and is presented here for the 3D case as well. Local concentrations of stresses during switching, as a result of the inter-granular effects, are thought to be the cause of micro-crack initiation along grain boundaries. For these reasons, a Direct Mesoscale Numerical Simulation (DMNS) of ferroelectric materials, using 3D MVCs is pursued in the present paper.

In the early days of finite element research (1960-2000), the hybrid stress formulation of Pian (1964), which uses interpolations for an equilibrated stress-field in the interior of a finite-element and inter-element compatible displacement fields only at the boundary of the element, was thought to be the only way of developing the stiffness matrices of arbitrary shaped finite elements (polygons with arbitrary number of sides in 2D, or polyhredra with arbitrary number of faces, each of which is an arbitrary polygon, in 3D) in 2 and 3 dimensions; and that the primal formulations which use only element-displacement field were unable to achieve inter-element compatibility. Subsequent work, as for instance in the text book by Atluri (2005), has shown that there are many other, perhaps simpler and more numerically stable, methods (which avoid the troublesome LBB conditions) for developing arbitrary shaped 2 and 3D Voronoi Cell elements, by using methods such as multi-field collocation methods, Trefftz Methods, Method of Fundamental Solutions, Radial Basis Function Methods, Symmetric Galerkin Boundary Element Methods, etc. These ideas to develop stable, invariant, and simple Voronoi Cells are pursued in the present paper, as well as in recent work by Bishay and Atluri (2012), and by Dong and Atluri (2011, 2012 a, b, c, d).

Sze and Sheng (2005) extended the Voronoi cell finite elements developed by Ghosh and his co-workers [Ghosh (2011)] based on Pian's hybrid stress finite element formulation [Pian (1964)] to model a ferroelectric polycrystalline. They used the Huo-Jiang single-crystal-multi-domain constitutive and switching model [Huo and Jiang (1997, 1998); Kim and Jiang (2002)]. Using this same framework, Jayabal *et al.* (2011) incorporated a micromechanical model based on well-established thermodynamic principles into the 2D Voronoi-cell finite elements. In their model, the switching process on the level of a single crystal of the overall ferroelectric polycrystalline is not continuous but faces a certain resistance or facilitation depending upon the changes in the combination of crystal variants.

The previously mentioned Voronoi-cell formulations for modeling ferroelectric materials are based on a multi-field hybrid electromechanical variational principle (modified principle of complementary energy, or Hellinger-Reissner variational principle [Sze and Pan (1999)]) and have the same disadvantages of Pian's hybrid elements, namely: (1) Lagrangian multipliers are involved in the multi-field

variational principle, and hence the derived elements suffer from the LBB stability conditions [Babuska (1973); Brezzi (1974)], which are impossible to be satisfied a priori, (2) there are additional matrices (**H** and **G**) which need to be computed through numerical quadrature in each element, (3) **H** needs to be inverted in each element, thus raising the computational cost, and the rank of **G** (equals to the number of the degrees of freedom in each element, less the number of rigid modes) in each element has to be assured a priori, (4) the use of "a priori equilibrated" stress field is difficult or even impossible for dynamical and geometrically nonlinear problems, (5) the assumed stress-field is often incomplete, and cannot account for the steep stress-gradients and singularities often encountered in microstructures with inclusions or voids, in multifunctional materials, and (6) prohibitive computational costs.

For elastic materials, Dong and Atluri (2012 a,b,c,d) developed 2D and 3D Trefftz Voronoi cell finite elements with voids and/or rigid/elastic inclusions for modeling heterogeneous materials. These elements were successful in accurately capturing the stress concentration around spherical/ellipsoidal voids/inclusions in composite and porous materials.

The Multiphysics Voronoi Cells (MVCs) presented here are the extensions of VCFEM-RBF developed in [Dong and Atluri (2011)] for 2D elasticity and VCFEM-RBF-W developed in [Bishay and Atluri (2012)] for 3D elasticity, by using Radial Basis Functions (RBF). The present MVCs are based on assuming internal as well as boundary fields separately for each of the primal variables (mechanical displacements and electric potential) and enforcing the compatibility between these fields. The compatibility between the interior and the boundary fields can be enforced using two methods. The first is done simply by collocating the interior and boundary fields at some boundary collocation-points, and the second is done by using the least square method which is the limit of the collocation method as the number of collocation points increases to infinity. For both the 2D and the 3D MVCs we assume the internal fields in terms of radial basis functions (RBF), while the boundary fields are assumed in terms of linear functions for the 2D case, and the linear Wachspress barycentric functions for the 3D case. Hence the 2D elements are denoted MVC-RBF and the 3D elements are denoted MVC-RBF-W. The present elements are much simpler and more efficient than Ghosh's hybrid-variational elements [Ghosh (2011)]. Also, the 3D MVC-RBF-W avoids adding additional nodes inside the boundary-surfaces through the use of Wachspress functions as the boundary surface displacements. However, Ghosh's formulation divides each surface of the 3D VCFEM into triangles, after adding a center node in each surface.

Each 2D MVC-RBF is a random irregular polygon, while the 3D MVC-RBF-W has an arbitrary number of faces, and each face has an arbitrary number of edges.

Considering only tetragonal unit cells composing the grains of a ferroelectric poly-crystalline, each crystal grain (or MVC) in 2D analysis has a randomly generated crystallographic axes (axes 1 and 3) and 4 possible constitutive-variants (or domain types) parallel and perpendicular to the crystallographic axis. While in the 3D analysis, we have 6 possible variants parallel and perpendicular to the three randomly generated crystallographic axes (axes 1, 2 and 3). When dealing with 3D models, the amount of computation is increased, hence it is important to adopt efficient constitutive and switching models. The Huo-Jiang single-crystal-multi-domain constitutive and switching model [Huo and Jiang (1997, 1998); Kim and Jiang (2002); Sze and Sheng (2005)] requires solving the finite element system not only once in each simulation step. The system is solved n times in each simulation step, where n is the number of switching elements (the elements that have tendency to switch). The final configuration of volume fractions in each element at any time step is the one that yields the minimum Gibbs free energy of the whole body. This method is obviously inefficient and impractical especially for 3D simulations with large numbers of elements. For this reason, representative volume element (RVE) is used in [Kim *et al.* (2003)] to incorporate this model in a 3D simulation. However, especially for ferroelectric polycrystalline samples, it is important to model the randomness of the grain shapes in order to simulate the local interactions and this cannot be done using RVE.

Any constitutive and switching models for ferroelectric materials can be incorporated with the developed MVCs to simulate the switching phenomenon. Here we use the switching model of [Jayabal *et al.* (2011)] which proved to be much more efficient than the previously mentioned models. It requires solving the VC system of equations just once in each simulation step. In consequence, the proposed modeling approach includes the essential intergranular effects in ferroelectric polycrystals arising from the individual grain geometries on the one hand, and the evolution of the underlying microstructures by switching effects on the other hand.

The rest of this paper is organized as follows: section 2 introduces the governing equations, and the method used to generate material matrices of each domain in each grain, or MVC, based on the orientation of the crystallographic axes of the grain. Section 3 presents the formulation of the 2D MVC-RBF and the 3D MVC-RBF-W used to model ferroelectric grains, and the method used to better condition the system of matrices to be solved. Section 4 is devoted for explaining the switching criteria and the kinetics, while in section 5, the solution method is illustrated. Section 6 presents the results of the 2D and 3D models in simulating ferroelectric and ferroelastic switching. Conclusions are summarized in section 7.

2 Governing equations

Adopting a matrix and vector notation, and denoting by $\mathbf{u}$ (3 components), $\boldsymbol{\sigma}$ (6 components) and $\boldsymbol{\varepsilon}$ (six components) the vectors of mechanical displacements, strains, and stresses respectively , and by φ (scalar), $\mathbf{E}$ (3 components) and $\mathbf{D}$ (3 components) the electric potential, electric field intensity vector, and the electric displacement vector, respectively, we have:

1- Stress equilibrium equations:

$$\boldsymbol{\partial_u}^T \boldsymbol{\sigma} + \bar{\mathbf{b}} = \mathbf{0}; \quad \boldsymbol{\sigma} = \boldsymbol{\sigma}^T \quad \text{in } \Omega \tag{1}$$

2- Charge conservation (Maxwell) equation:

$$\boldsymbol{\partial_e}^T \mathbf{D} - \overline{\rho_f} = 0, \quad \text{in } \Omega \tag{2}$$

Where Ω is the problem domain, $\bar{\mathbf{b}}$ is the body force, and $\overline{\rho_f}$ is the electric free charge density.

3- Strain-displacement equations:

$$\boldsymbol{\varepsilon} = \boldsymbol{\partial_u u} \tag{3}$$

4- Electric field intensity- electric potential equations:

$$\mathbf{E} = -\boldsymbol{\partial_e}\varphi \tag{4}$$

Where

$$\boldsymbol{\partial_u} = \begin{bmatrix} \frac{\partial}{\partial x_1} & 0 & 0 & \frac{\partial}{\partial x_2} & 0 & \frac{\partial}{\partial x_3} \\ 0 & \frac{\partial}{\partial x_2} & 0 & \frac{\partial}{\partial x_1} & \frac{\partial}{\partial x_3} & 0 \\ 0 & 0 & \frac{\partial}{\partial x_3} & 0 & \frac{\partial}{\partial x_2} & \frac{\partial}{\partial x_1} \end{bmatrix}^T, \quad \boldsymbol{\partial_e} = \begin{bmatrix} \frac{\partial}{\partial x_1} & \frac{\partial}{\partial x_2} & \frac{\partial}{\partial x_3} \end{bmatrix}^T$$

This representation of the electric field intensity (Eq. 4), as gradients of the electric potential guarantees the satisfaction of the other Maxwell equations ($\nabla \times \mathbf{E} = \mathbf{0}$).

5- Constitutive relations for the type-*i*-domain in a ferroelectric material:

$$\begin{aligned} \boldsymbol{\varepsilon}_i &= \mathbf{S}_i \boldsymbol{\sigma}_i + \mathbf{m}_i^T \mathbf{E}_i + \boldsymbol{\varepsilon}_i^{\mathbf{S}} \\ \mathbf{D}_i &= \mathbf{m}_i \boldsymbol{\sigma}_i + \mathbf{d}_i^T \mathbf{E}_i + \mathbf{P}_i^{\mathbf{S}} \end{aligned} \tag{5}$$

Where $\boldsymbol{\varepsilon}_i$ and $\boldsymbol{\sigma}_i$ are, respectively, the strain and stress tensors, and $\mathbf{E}_i$ and $\mathbf{D}_i$ are the electric field intensity and electric displacement vectors of type-*i*-domain; $\boldsymbol{\varepsilon}_i^{\mathbf{S}}$

and $\mathbf{P}_i^{\mathbf{S}}$ are the spontaneous strain tensor and spontaneous polarization vector of type-i-domain, respectively; $\mathbf{S}_i$, $\mathbf{m}_i$, $\mathbf{d}_i$ are, respectively, the elastic compliance tensor measured under constant electric field, piezoelectric and dielectric tensors measured under constant stress of type-i-domain.

For three-dimensional analysis, there are six possible spontaneous polarization directions in a tetragonal unit cell. These directions are parallel/opposite to the crystal axes which are denoted as the 1-, 2- and 3- directions. But for two-dimensional analysis, there are only four possible spontaneous polarization directions. The crystallographic axes are the reference directions for expressing all the constitutive relations. As a result, each crystal grain in a polycrystalline ferroelectric material has six different types of domains in a 3D analysis, and four types in a 2D analysis.

To determine the average physical properties of a ferroelectric crystal grain (or Multiphysics Voronoi Cell MVC), a simple averaging method is used. The method is based on the assumptions that all the domains in a crystal grain are subjected to uniform stress and electric field intensity, and that the strain and electric displacement of the crystal grain are the summation of those of all the domains of the crystal grain weighted by their volume fractions c_is, i.e.

$$\boldsymbol{\sigma}_i = \boldsymbol{\sigma}, \quad \mathbf{E}_i = \mathbf{E}, \quad \boldsymbol{\varepsilon} = \sum_{i=1}^{N_d} c_i \boldsymbol{\varepsilon}_i, \quad \mathbf{D} = \sum_{i=1}^{N_d} c_i \mathbf{D}_i \tag{6}$$

Where N_d is the number of domain types in the crystal grain (4 for 2D analysis and 6 for 3D analysis, considering only ferroelectric materials entirely composed of tetragonal unit cells). The volume fractions, c_is, should always satisfy the consistency conditions:

$$c_i \geq 0, \quad \sum_{i=1}^{N_d} \dot{c}_i = 1, \quad \sum_{i=1}^{N_d} c_i = 0 \tag{7}$$

Substituting Eq. 6 into Eq. 5, we get the constitutive equation for a ferroelectric crystal grain as:

$$\begin{Bmatrix} \boldsymbol{\varepsilon} \\ \mathbf{D} \end{Bmatrix} = \begin{bmatrix} \mathbf{S} & \mathbf{m}^T \\ \mathbf{m} & \mathbf{d} \end{bmatrix} \begin{Bmatrix} \boldsymbol{\sigma} \\ \mathbf{E} \end{Bmatrix} + \begin{Bmatrix} \boldsymbol{\varepsilon}^{\mathbf{R}} \\ \mathbf{P}^{\mathbf{R}} \end{Bmatrix} = \begin{Bmatrix} \boldsymbol{\varepsilon}^{\mathbf{L}} \\ \mathbf{D}^{\mathbf{L}} \end{Bmatrix} + \begin{Bmatrix} \boldsymbol{\varepsilon}^{\mathbf{R}} \\ \mathbf{P}^{\mathbf{R}} \end{Bmatrix} \tag{8}$$

Where

$$\boldsymbol{\varepsilon}^{\mathbf{R}} = \sum_{i=1}^{N_d} c_i \boldsymbol{\varepsilon}_i^{\mathbf{S}}, \quad \mathbf{P}^{\mathbf{R}} = \sum_{i=1}^{N_d} c_i \mathbf{P}_i^{\mathbf{S}}, \quad \mathbf{S} = \sum_{i=1}^{N_d} c_i \mathbf{S}_i, \quad \mathbf{m} = \sum_{i=1}^{N_d} c_i \mathbf{m}_i, \quad \mathbf{d} = \sum_{i=1}^{N_d} c_i \mathbf{d}_i \tag{9}$$

Here $\boldsymbol{\varepsilon}$,$\boldsymbol{\sigma}$, $\mathbf{E}$ and $\mathbf{D}$ are the average vectors of strain, stress, electric field intensity and electric displacement in the crystal grain (MVC) respectively; $\boldsymbol{\varepsilon}^{\mathbf{L}}$ and $\mathbf{D}^{\mathbf{L}}$ are

the average linear (reversible) strain and electric displacement vectors respectively; $\boldsymbol{\varepsilon}^{\mathbf{R}}$ and $\mathbf{P^R}$ are the average remnant (irreversible) strain and polarization vectors respectively; $\mathbf{S}$, $\mathbf{m}$ and $\mathbf{d}$ are the average material matrices for the grain or VC in question.

Eq. 5 can also be written as:

$$\boldsymbol{\sigma}_i = \mathbf{C}_i(\boldsymbol{\varepsilon}_i - \boldsymbol{\varepsilon}_i^{\mathbf{S}}) - \mathbf{e}_i^T \mathbf{E}_i$$
$$\mathbf{D}_i = \mathbf{e}_i(\boldsymbol{\varepsilon}_i - \boldsymbol{\varepsilon}_i^{\mathbf{S}}) + \mathbf{h}_i^T \mathbf{E}_i + \mathbf{P}_i^{\mathbf{S}} \tag{10}$$

Where $\mathbf{C}_i = \mathbf{S}_i^{-1}$, $\mathbf{e}_i = \mathbf{m}_i\mathbf{C}_i$ and $\mathbf{h}_i = \mathbf{d}_i - \mathbf{m}_i\mathbf{e}_i^T$ are the elastic tensor measured under constant electric field, piezoelectric and dielectric tensors measured under constant strain of the type-i-domain. Again the elastic and piezoelectric tensors can be cast in a matrix form.

Similarly the constitutive equation for the ferroelectric crystal grain (MVC), Eq. 8, can be written as:

$$\begin{Bmatrix} \boldsymbol{\sigma} \\ \mathbf{D} \end{Bmatrix} = \begin{bmatrix} \mathbf{C} & \mathbf{e}^T \\ \mathbf{e} & -\mathbf{h} \end{bmatrix} \begin{Bmatrix} \boldsymbol{\varepsilon} - \boldsymbol{\varepsilon}^{\mathbf{R}} \\ -\mathbf{E} \end{Bmatrix} + \begin{Bmatrix} \mathbf{0} \\ \mathbf{P^R} \end{Bmatrix} \tag{11}$$

With $\mathbf{C} = \mathbf{S}^{-1}$, $\mathbf{e} = \mathbf{mC}$ and $\mathbf{h} = \mathbf{d} - \mathbf{me}^T$.

Usually $\mathbf{C}_i$, $\mathbf{e}_i$ and $\mathbf{h}_i$ are the given material properties. From them we can get $\mathbf{S}_i = \mathbf{C}_i^{-1}$, $\mathbf{m}_i = \mathbf{e}_i\mathbf{C}_i^{-1}$ and $\mathbf{d}_i = \mathbf{h}_i + \mathbf{m}_i\mathbf{e}_i^T = \mathbf{h}_i + \mathbf{e}_i\mathbf{C}_i^{-1}\mathbf{e}_i^T$. Then we can get the average material matrices $\mathbf{S}$, $\mathbf{m}$ and $\mathbf{d}$ using Eq. 9 and $\mathbf{C}$, $\mathbf{e}$ and $\mathbf{h}$ using Eq. 11.

If the spontaneous (irreversible) strain and polarization are assumed to vanish, we then get the linear constitutive equations in the piezoelectric response region:

$$\begin{Bmatrix} \boldsymbol{\varepsilon}^{\mathbf{R}} \\ \mathbf{P^R} \end{Bmatrix} = \begin{Bmatrix} \mathbf{0} \\ \mathbf{0} \end{Bmatrix}, \quad \begin{Bmatrix} \boldsymbol{\varepsilon} \\ \mathbf{D} \end{Bmatrix} = \begin{Bmatrix} \boldsymbol{\varepsilon}^{\mathbf{L}} \\ \mathbf{D^L} \end{Bmatrix} = \begin{bmatrix} \mathbf{S} & \mathbf{m}^T \\ \mathbf{m} & \mathbf{d} \end{bmatrix} \begin{Bmatrix} \boldsymbol{\sigma} \\ \mathbf{E} \end{Bmatrix},$$
$$\text{or} \quad \begin{Bmatrix} \boldsymbol{\sigma} \\ \mathbf{D^L} \end{Bmatrix} = \begin{bmatrix} \mathbf{C} & \mathbf{e}^T \\ \mathbf{e} & -\mathbf{h} \end{bmatrix} \begin{Bmatrix} \boldsymbol{\varepsilon}^{\mathbf{L}} \\ -\mathbf{E} \end{Bmatrix} \tag{12}$$

6- First and second laws of thermodynamics for deformable electric materials:

$$\rho\dot{U} = \boldsymbol{\sigma} : \dot{\boldsymbol{\varepsilon}} + \mathbf{E} \cdot \dot{\mathbf{D}} - \nabla \cdot \mathbf{r}, \tag{13}$$

$$\rho\dot{\eta} - \nabla \cdot \left(\frac{\mathbf{r}}{T}\right) \geq 0 \tag{14}$$

Where ρ, U, $\mathbf{r}$, η and T denote the density, the internal energy per unit mass, the heat flux, the entropy per unit mass and the absolute temperature. Super-script dot denotes material time derivative.

The SI units of the mentioned fields are as follows: stress $\boldsymbol{\sigma}$ (Pa or N/m^2), strains $\boldsymbol{\varepsilon}$,

$\boldsymbol{\varepsilon}^{\mathbf{L}}$ and $\boldsymbol{\varepsilon}^{\mathbf{R}}$ (No unit or m/m), electric displacements $\mathbf{D}$, $\mathbf{D}^{\mathbf{L}}$ and $\mathbf{P}^{\mathbf{R}}$ (C/m^2), electric field intensity $\mathbf{E}$ (V/m or N/C), and the SI units of the material matrices are: material elastic stiffness $\mathbf{C}$ (Pa or N/m^2), piezoelectric matrix $\mathbf{e}$ (C/m^2), and dielectric matrix $\mathbf{h}$ (C/Vm). Finally the SI unit of the density ρ (Kg/m^3), internal energy per unit mass U (J/Kg), the heat flux $\mathbf{r}$ (J/m^2), the entropy per unit mass, η (J/(Kg.K)), and the absolute temperature, T (K).

7- Mechanical natural (traction) boundary conditions:

$$\mathbf{n_\sigma}\boldsymbol{\sigma} = \bar{\mathbf{t}} \quad \text{at } S_t, \tag{15}$$

8- Mechanical essential (displacement) boundary conditions:

$$u_i = \bar{u}_i \quad \text{at } S_u, \tag{16}$$

9- Electric natural boundary conditions:

$$\mathbf{n_e}\mathbf{D} = \overline{Q} \quad \text{at } S_Q, \tag{17}$$

10- Electric essential boundary conditions:

$$\varphi = \overline{\varphi} \quad \text{at } S_\varphi, \tag{18}$$

where

$$\mathbf{n_\sigma} = \begin{bmatrix} n_x & 0 & 0 & n_y & 0 & n_z \\ 0 & n_y & 0 & n_x & n_z & 0 \\ 0 & 0 & n_z & 0 & n_y & n_x \end{bmatrix} \quad \mathbf{n_e} = \begin{bmatrix} n_x & n_y & n_z \end{bmatrix}$$

$\bar{\mathbf{t}}$ is the boundary traction vector, $\overline{Q}$ is the specified surface density of free charge. n_x, n_y and n_z , the three components of $\mathbf{n_\sigma}$ and $\mathbf{n_e}$, are the components of the unit outward normal to the boundaries S_t or S_Q. $\bar{\mathbf{u}}$ is the specified mechanical displacement vector at the boundary S_u , and $\overline{\varphi}$ is the specified electric potential at the boundary S_φ.

When dividing the whole domain of the body into subdomains (MVCs), the following conditions should also be satisfied at each subdomain interface S_m:

1- Mechanical (displacement) compatibility at each inter-subdomain boundary:

$$u_i{}^+ = u_i{}^- \quad \text{at } S_m, \tag{19}$$

2- Mechanical (traction) reciprocity condition at each inter-subdomain boundary:

$$(\mathbf{n_\sigma}\boldsymbol{\sigma})^+ + (\mathbf{n_\sigma}\boldsymbol{\sigma})^- = 0 \quad \text{at } S_m, \tag{20}$$

3- Electric potential compatibility at each inter-subdomain boundary:

$$\varphi^+ = \varphi^- \quad \text{at } S_m, \tag{21}$$

4- Electric reciprocity condition at each inter-subdomain boundary:

$$(\mathbf{n_e D})^+ + (\mathbf{n_e D})^- = 0 \quad \text{at } S_m, \tag{22}$$

2.1 Material properties for the different domain types

For the 3D case, domains of types 1 and 2 with the spontaneous polarization direction along the $\pm$ crystal axis 3, the material properties with respect to the crystallographic axes $x'_1 - x'_2 - x'_3$ can be written as:

$$\mathbf{C}_i = \begin{bmatrix} C_{11} & C_{12} & C_{13} & 0 & 0 & 0 \\ C_{12} & C_{11} & C_{13} & 0 & 0 & 0 \\ C_{13} & C_{13} & C_{33} & 0 & 0 & 0 \\ 0 & 0 & 0 & C_{44} & 0 & 0 \\ 0 & 0 & 0 & 0 & C_{44} & 0 \\ 0 & 0 & 0 & 0 & 0 & C_{66} \end{bmatrix}, \quad \boldsymbol{\varepsilon}_i^S = \begin{Bmatrix} \varepsilon_{11}^S \\ \varepsilon_{11}^S \\ \varepsilon_{33}^S \\ 0 \\ 0 \\ 0 \end{Bmatrix}, \quad \mathbf{P}_i^S = \begin{Bmatrix} 0 \\ 0 \\ \pm p^S \end{Bmatrix} \tag{23}$$

$$\mathbf{e}_i = \pm \begin{bmatrix} 0 & 0 & 0 & 0 & e_{15} & 0 \\ 0 & 0 & 0 & e_{15} & 0 & 0 \\ e_{31} & e_{31} & e_{33} & 0 & 0 & 0 \end{bmatrix}, \quad \mathbf{h}_i = \begin{bmatrix} h_{11} & 0 & 0 \\ 0 & h_{11} & 0 \\ 0 & 0 & h_{33} \end{bmatrix}$$

Denoting the unit vectors of the local crystal orthogonal coordinate system $(x'_1 - x'_2 - x'_3)$ as $\mathbf{g}'_1$, $\mathbf{g}'_2$ and $\mathbf{g}'_3$, all the tensors of the material properties can be rotated to any other orthogonal coordinate system $(x_1 - x_2 - x_3)$ whose unit vectors are $\mathbf{g}_1$, $\mathbf{g}_2$ and $\mathbf{g}_3$ using the rotation matrix $\mathbf{R}$:

$$\mathbf{x} = \mathbf{R}\mathbf{x}', \quad \mathbf{g}_k = \mathbf{R}\mathbf{g}'_k, \tag{24}$$

Where $R_{kl} = \mathbf{g}_k \cdot \mathbf{g}'_l$ and $\mathbf{R} = R_{kl}\mathbf{g}_k\mathbf{g}'_l$.
For 2D rotation around x_2-axis by angle θ, $\mathbf{R}$ has the form:

$$\mathbf{R} = \begin{bmatrix} \cos(\theta) & 0 & -\sin(\theta) \\ 0 & 1 & 0 \\ \sin(\theta) & 0 & \cos(\theta) \end{bmatrix} \tag{25}$$

For 3D rotation characterized by the three Euler angles (θ, ϕ, ψ), the rotations are done according to the following sequence: rotation by angle θ around x_3-axis to get $x'''_1 - x'''_2 - x'''_3$ coordinate axes, then rotation by angle ϕ around the new x'''_1-axis to get $x''_1 - x''_2 - x''_3$ coordinate axes, followed by rotation by angle ψ around the new

x_3''-axis to get $x_1' - x_2' - x_3'$ coordinate axes. This is shown in Fig. 1. **R** in this case can be written as:

$$\mathbf{R} = \begin{bmatrix} c(\psi) & -s(\psi) & 0 \\ s(\psi) & c(\psi) & 0 \\ 0 & 0 & 1 \end{bmatrix} \begin{bmatrix} 1 & 0 & 0 \\ 0 & c(\phi) & -s(\phi) \\ 0 & s(\phi) & c(\phi) \end{bmatrix} \begin{bmatrix} c(\theta) & -s(\theta) & 0 \\ s(\theta) & c(\theta) & 0 \\ 0 & 0 & 1 \end{bmatrix} \tag{26}$$

Where c( ) means cos( ) and s( ) means sin( ).
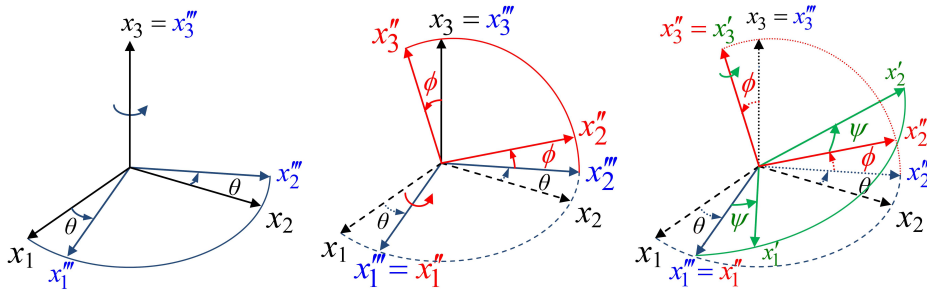
Figure 1: 3D rotation of axes using Euler angles: (left) rotation by angle θ around x_3-axis, (middle) rotation by angle ϕ around x_1'''-axis, (right) rotation by angle ψ around x_3''-axis

.

For any material tensor, such as the elastic stiffness tensor (which is a fourth order tensor), the components of the tensor in the new coordinate axes can be expressed in terms of the components in the old coordinate system as follows:

$$\begin{aligned} \mathbf{C} &= C'_{pqrs} \mathbf{g}'_p \mathbf{g}'_q \mathbf{g}'_r \mathbf{g}'_s = C_{ijkl} \mathbf{g}_i \mathbf{g}_j \mathbf{g}_k \mathbf{g}_l, \\ C_{ijkl} &= C'_{pqrs} (\mathbf{g}'_p \cdot \mathbf{g}_i)(\mathbf{g}'_q \cdot \mathbf{g}_j)(\mathbf{g}'_r \cdot \mathbf{g}_k)(\mathbf{g}'_s \cdot \mathbf{g}_l) \end{aligned} \tag{27}$$

So domains of types 3 and 4 with the spontaneous polarization direction along the $\pm$ crystal axis 1, the material properties with respect to the crystallographic axes $x_1' - x_2' - x_3'$ can be obtained by a rotation of $\pm\,90°$ around x_2'- axis (using the rotation matrix in Eq. 25). Domains of types 5 and 6 with the spontaneous polarization direction along the $\pm$ crystal axis 2, the material properties with respect to the crystallographic axes $x_1' - x_2' - x_3'$ can be obtained by a rotation of $\pm\,90°$ around x_1'- axis (using the rotation matrix in Eq. 26 with $\theta = \psi = 0$).

For the 2D case, if the body is very long (infinite) in the 2-direction (plane strain case), then we have the assumptions:

$$\varepsilon_2 = \varepsilon_4 = \varepsilon_6 = 0, \quad E_2 = 0, \quad \text{and} \quad \varepsilon_2^S = 0, \quad P_2^S = 0 \tag{28}$$

This reduces the problem into 2D case in the $X_1 - X_3$ plane with only 4 types of domains (types 1,2, 3 and 4). In this case, the material matrices in Eq. 23 of domain types 1 and 2, with the spontaneous polarization direction along the $\pm$ crystal axis 3, reduce to:

$$\mathbf{C}_i = \begin{bmatrix} C_{11} & C_{13} & 0 \\ C_{13} & C_{33} & 0 \\ 0 & 0 & C_{44} \end{bmatrix}, \quad \boldsymbol{\varepsilon}_i^{\mathbf{S}} = \begin{Bmatrix} \varepsilon_{11}^S \\ \varepsilon_{33}^S \\ 0 \end{Bmatrix}, \quad \mathbf{P}_i^{\mathbf{S}} = \begin{Bmatrix} 0 \\ \pm p^S \end{Bmatrix}$$

$$\mathbf{e}_i = \pm \begin{bmatrix} 0 & 0 & e_{15} \\ e_{31} & e_{33} & 0 \end{bmatrix}, \quad \mathbf{h}_i = \begin{bmatrix} h_{11} & 0 \\ 0 & h_{33} \end{bmatrix}$$

(29)

The material properties of the domains of types 3 and 4, with the spontaneous polarization direction along the $\pm$ crystal axis 1, reduce similarly from the matrices of the 3D case.

When dealing with polycrystalline ferroelectric ceramic with many grains of arbitrary shapes, the crystallographic coordinate system is randomly oriented in each grain. Hence, with respect to the global coordinate axis $(X_1 - X_2 - X_3)$ of the aggregate, the material properties of each domain inside a grain can also be obtained using the rotation matrix $\mathbf{R}$, where the angle θ in Eq. 25 for the 2D case, or the angles θ, ϕ and ψ in Eq. 26 for the 3D case, are between the global coordinate system and the local crystallographic coordinate system of the grain. Fig. 2 shows the global coordinate system and the crystallographic axes of the grain with the polarization directions of the 6 possible domain types in a ferroelectric crystal grain aligned with the crystallographic axes.
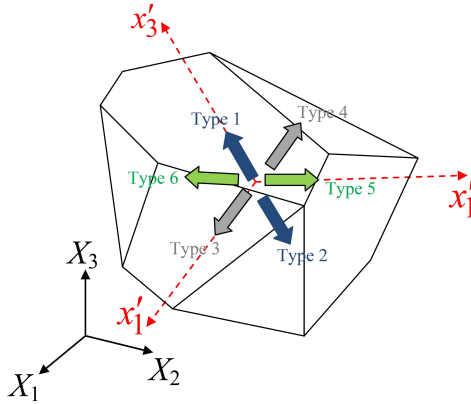

Figure 2: Crystallographic axes in a ferroelectric crystal grain and the polarization direction of the 6 possible domain types or variants

3   Multiphysics Voronoi Cell (MVC) formulation for ferroelectric materials

Discretizing the problem domain using the 2D or the 3D Voronoi cells (MVCs), so that each element has a unique shape, will allow us to study micromechanical problems with ferroelectric materials, since the shapes and the sizes of the grains in the micro-scale are random and the Voronoi cells are the best approximation for this structure due to randomness it provide to the element shapes and sizes. Each grain (or MVC) is surrounded by a varying number of differently shaped neighboring grains. Dirichlet tessellation of the domain into MVCs together with randomly generated crystallographic axes for each grain, in general, represents the overall polycrystalline microstructure better. The 2D grain, VC-RBF-1 and VC-RBF-2, based on radial basis functions presented in [Dong and Atluri (2011)], and the 3D Voronoi cells element, VC-RBF-W, based on radial basis functions and Washspress functions presented in [Bishay and Atluri (2012)] for elasticity, are extended here for modeling the multiphysics of ferroelectric materials.

3.1   Interior and boundary primal variables

Defining the mechanical displacement and electric potential fields using radial basis functions (RBF) in Ω_m the interior of each element, and as linear functions on $\partial\Omega_m$ the boundary of each element, we can write the internal fields as:

$$
\begin{aligned}
u_i^I &= \mathbf{R}^T(\mathbf{x})\mathbf{a}_{\mathbf{u}i} + \mathbf{P}^T(\mathbf{x})\mathbf{b}_{\mathbf{u}i} \quad \text{in } \Omega_m \\
\varphi^I &= \mathbf{R}^T(\mathbf{x})\mathbf{a}_{\boldsymbol{\varphi}} + \mathbf{P}^T(\mathbf{x})\mathbf{b}_{\boldsymbol{\varphi}} \quad \text{in } \Omega_m
\end{aligned}
\tag{30}
$$

or,

$$
u_i^I = \mathbf{M}(\mathbf{x})\boldsymbol{\alpha}_{\mathbf{u}i}, \quad \varphi^I = \mathbf{M}(\mathbf{x})\boldsymbol{\alpha}_{\boldsymbol{\varphi}}, \quad \text{in } \Omega_m
\tag{31}
$$

Where $\mathbf{M}(\mathbf{x}) = [\mathbf{R}^T(\mathbf{x}) \quad \mathbf{P}^T(\mathbf{x})]$ and $\boldsymbol{\alpha}_{\mathbf{u}i} = \begin{Bmatrix} \mathbf{a}_{\mathbf{u}i} \\ \mathbf{b}_{\mathbf{u}i} \end{Bmatrix}$, $\boldsymbol{\alpha}_{\boldsymbol{\varphi}} = \begin{Bmatrix} \mathbf{a}_{\boldsymbol{\varphi}} \\ \mathbf{b}_{\boldsymbol{\varphi}} \end{Bmatrix}$, $i = 1,3$

and $\mathbf{R}^\mathbf{T}(\mathbf{x}) = [R^{r1}(\mathbf{x}) \; R^{r2}(\mathbf{x}) \; ... \; R^{rl}(\mathbf{x})]$ is a set of radial basis functions centered at l points $\mathbf{x}^{r1}, \mathbf{x}^{r2}, ... \mathbf{x}^{rl}$ along $\partial\Omega_m$; $\mathbf{P}^\mathbf{T}(\mathbf{x}) = [P^1(\mathbf{x}) \; P^2(\mathbf{x}) \; ... P^m(\mathbf{x})]$ is a set of m monomial functions which are complete to a certain order; $\mathbf{a}_{\mathbf{u}i}, \mathbf{b}_{\mathbf{u}i}, \mathbf{a}_{\boldsymbol{\varphi}}$ and $\mathbf{b}_{\boldsymbol{\varphi}}$ are coefficient vectors.

The radial basis functions used here have the form:

$$
R^{rl}(\mathbf{x}) = \begin{cases} \left(1 - \frac{d^{rl}(\mathbf{x})}{r^{rl}}\right)^3 \left(1 + 3\frac{d^{rl}(\mathbf{x})}{r^{rl}}\right), & d^{rl}(\mathbf{x}) < r^{rl} \\ 0, & d^{rl}(\mathbf{x}) \geq r^{rl} \end{cases}
\tag{32}
$$

Where $d^{rl}(\mathbf{x}) = |\mathbf{x} - \mathbf{x}^{rl}|$ is the Euclidean distance from point $\mathbf{x}$ to point $\mathbf{x}^{rl}$, r^{rl} is the support size of $R^{rl}(\mathbf{x})$.

In this study, a first order complete polynomial basis is used:

$$\mathbf{P}^T(\mathbf{x}) = \begin{bmatrix} 1 & x_1 & x_2 \end{bmatrix} \quad \text{for 2D analysis}$$
$$\mathbf{P}^T(\mathbf{x}) = \begin{bmatrix} 1 & x_1 & x_2 & x_3 \end{bmatrix} \quad \text{for 3D analysis}$$

(33)

The linear boundary fields can generally be written, in terms of the nodal values of the mechanical displacements $\mathbf{q_{u}}_i$ and electric potential $\mathbf{q_\phi}$, as:

$$u_i^B = \tilde{\mathbf{N}}\mathbf{q_{u}}_i, \quad \varphi_i^B = \tilde{\mathbf{N}}\mathbf{q_\phi} \quad \text{on } \partial\Omega_m \tag{34}$$

In the 2D version of the MVC-RBF (see Fig. 3), we use simple linear shape functions:

$$\tilde{\mathbf{N}} = \frac{1}{2}[1 - \xi \quad 1 + \xi] \tag{35}$$

Where $-1 \leq \xi \leq 1$ is the normalized running length from one corner to the other on each side of the boundary. While in the 3D version, denoted by MVC-RBF-
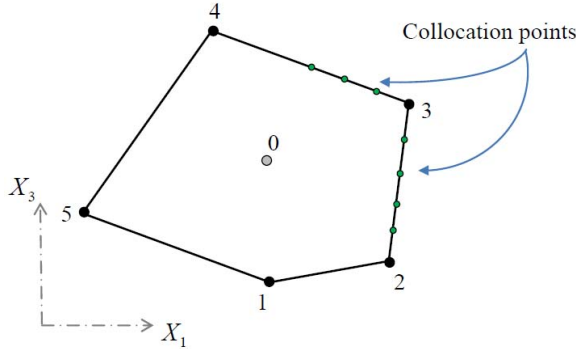

Figure 3: 2D irregular polygon (Voronoi cell)

.

W, the element is an arbitrary polyhedron (3D Voronoi Cell) in the 3D space, as shown in Fig. 4, with n nodes $\mathbf{x_1}, \mathbf{x_2}, ...\mathbf{x_n}$, and corresponding nodal displacements $u_i^1, u_i^2, ...u_i^n$. A smooth linear displacement field assumption on each surface can be used as:

$$\tilde{\mathbf{N}} = [\lambda_1(\mathbf{x}) \quad \lambda_2(\mathbf{x}) \quad \lambda_3(\mathbf{x}) \quad ...] \tag{36}$$

Dealing with polygonal surfaces, Barycentric coordinates should be used to describe the displacement field. The Barycentric coordinates, denoted as λ_i ($i = 1, 2, ..n$) where n is the number of the vertices of the convex polygon, in general should satisfy two properties:
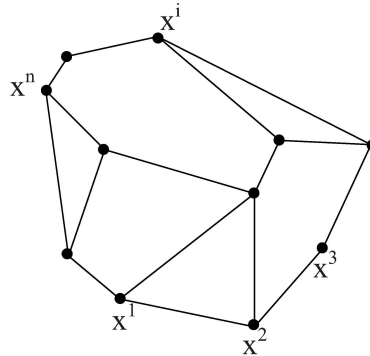
Figure 4: Polyhedron (3D Voronoi cell) element with arbitrary number of polygonal faces

.

1. Non-negative: $\lambda_i \geq 0$ on $\partial\Omega_m$.

2. Linear completeness: For any linear function $f(\mathbf{x}) : \partial\Omega_m \to \mathbb{R}$,
   $f(\mathbf{x}) = \sum_{i=1}^{n} f(\mathbf{x^i})\lambda_i$.

Any set of Barycentric coordinates under this definition also satisfies:

1. Partition of unity: $\sum_{i=1}^{n} \lambda_i \equiv 1$.

2. Linear precision: $\sum_{i=1}^{n} \mathbf{x^i}\lambda_i(\mathbf{x}) = \mathbf{x}$.

3. Dirac delta: $\lambda_i(\mathbf{x^j}) = \delta_{ij}$

In this work, we use the Wachspress coordinates [Wachspress (1975)], defined as follows:
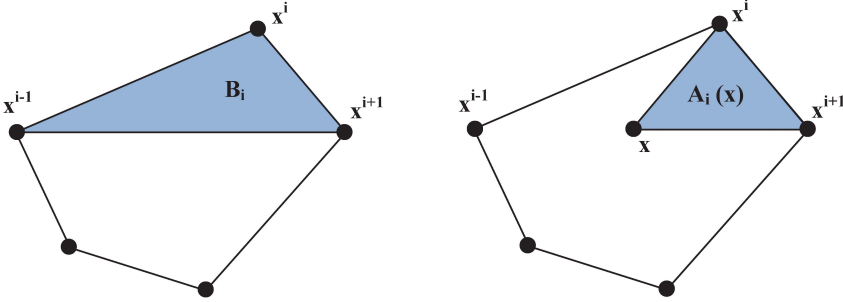
Let $\mathbf{x} \in \partial\Omega_m$ and define the areas: B_i as the area of the triangle having $\mathbf{x^{i-1}}, \mathbf{x^i}$ and $\mathbf{x^{i+1}}$ as its three vertices, and $A_i(\mathbf{x})$ as the area of the triangle having $\mathbf{x}, \mathbf{x^i}$ and $\mathbf{x^{i+1}}$ as its three vertices. This is illustrated in Fig. 5.

Define the Wachspress weight function as:

$$w_i(\mathbf{x}) = B_i \prod_{j \neq i, i-1} A_j(\mathbf{x}) \tag{37}$$

Then, the Wachspress coordinates are given by the rational functions:

$$\lambda_i(\mathbf{x}) = \frac{w_i(\mathbf{x})}{\sum_{j=1}^{n} w_j(\mathbf{x})} \tag{38}$$

Figure 5: Definition of triangles B_i and $A_i(\mathbf{x})$

Similar to the well-known triangular coordinates used in the 2D triangular elements, where the shape functions associated with the three vertices are indeed the triangular coordinates themselves, the shape functions associated with the vertices of this polygonal surface displacement field are the Barycentric coordinates. The triangular coordinates are actually a special case of the Barycentric coordinates when the polygon is just a triangle.

The compatibility between the interior fields , as in Eq. 31 and the boundary fields, as in equation Eq. 34, at the surface $\partial \Omega_m$,in each element can be enforced in many ways, including:

(a) The boundary collocation between (u_i^I, φ^I) and (u_i^B, φ^B) at selected points on $\partial \Omega_m$, , or

(b) The method of minimizing boundary-least-square error between (u_i^I, φ^I) and (u_i^B, φ^B) at $\partial \Omega_m$.

Both methods are presented in the following:

Using the Collocation method:

The coefficients $\boldsymbol{\alpha}_{\mathbf{u}i}$ and $\boldsymbol{\alpha}_{\boldsymbol{\varphi}}$ are obtained by enforcing the compatibility condition of the interior and the boundary fields at collocation points $\mathbf{x}^{r1}, \mathbf{x}^{r2}, ..., \mathbf{x}^{rn}$ (see Fig. 3 for the 2D case and Fig. 6 (left) for the 3D case). This leads to:

$$\begin{bmatrix} \mathbf{R_0} & \mathbf{P_0} \\ \mathbf{P_0}^T & \mathbf{0} \end{bmatrix} \begin{Bmatrix} \mathbf{a}_{\mathbf{u}i} \\ \mathbf{b}_{\mathbf{u}i} \end{Bmatrix} = \begin{Bmatrix} \mathbf{u}_i^{Br} \\ \mathbf{0} \end{Bmatrix}, \quad \begin{bmatrix} \mathbf{R_0} & \mathbf{P_0} \\ \mathbf{P_0}^T & \mathbf{0} \end{bmatrix} \begin{Bmatrix} \mathbf{a}_{\boldsymbol{\varphi}} \\ \mathbf{b}_{\boldsymbol{\varphi}} \end{Bmatrix} = \begin{Bmatrix} \boldsymbol{\varphi}^{Br} \\ \mathbf{0} \end{Bmatrix} \tag{39}$$

$$\mathbf{R_0} = \begin{bmatrix} R^{r1}(\mathbf{x}^{r1}) & R^{r2}(\mathbf{x}^{r1}) & ... & R^{rl}(\mathbf{x}^{r1}) \\ R^{r1}(\mathbf{x}^{r2}) & R^{r2}(\mathbf{x}^{r2}) & ... & R^{rl}(\mathbf{x}^{r2}) \\ \vdots & \vdots & \vdots & \vdots \\ R^{r1}(\mathbf{x}^{rl}) & R^{r2}(\mathbf{x}^{rl}) & ... & R^{rl}(\mathbf{x}^{rl}) \end{bmatrix} \tag{40}$$
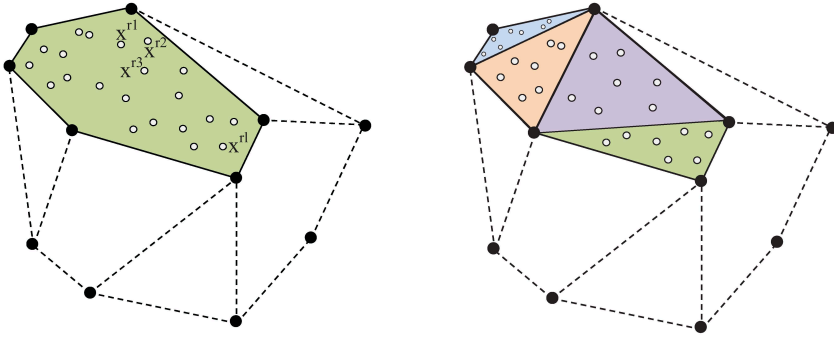
Figure 6: (left) collocation points on one boundary surface of the 3D MVC-RBF-W. (right) triangulating each boundary surface and taking the Gaussian points in each triangle to be the RBF centers and collocation points

$$
\mathbf{P_0} = \begin{bmatrix} P^1(\mathbf{x}^{r1}) & P^2(\mathbf{x}^{r1}) & ... & P^l(\mathbf{x}^{r1}) \\ P^1(\mathbf{x}^{r2}) & P^2(\mathbf{x}^{r2}) & ... & P^l(\mathbf{x}^{r2}) \\ \vdots & \vdots & \vdots & \vdots \\ P^1(\mathbf{x}^{rl}) & P^2(\mathbf{x}^{rl}) & ... & P^l(\mathbf{x}^{rl}) \end{bmatrix} \tag{41}
$$

$$
\begin{aligned}
(\mathbf{u}_i^{\mathbf{B}r})^T &= [u_i^{Br1} \quad u_i^{Br2} \quad ... \quad u_i^{Brl}] \\
&= \left[\sum_{k=1}^n \tilde{N}^k(\mathbf{x}^{r1})u_i^k \quad \sum_{k=1}^n \tilde{N}^k(\mathbf{x}^{r2})u_i^k \quad ... \quad \sum_{k=1}^n \tilde{N}^k(\mathbf{x}^{rl})u_i^k \right] \\
(\boldsymbol{\varphi}^{\mathbf{B}r})^T &= [\varphi^{Br1} \quad \varphi^{Br2} \quad ... \quad \varphi^{Brl}] \\
&= \left[\sum_{k=1}^n \tilde{N}^k(\mathbf{x}^{r1})\varphi^k \quad \sum_{k=1}^n \tilde{N}^k(\mathbf{x}^{r2})\varphi^k \quad ... \quad \sum_{k=1}^n \tilde{N}^k(\mathbf{x}^{rl})\varphi^k \right]
\end{aligned} \tag{42}
$$

Solving equation (39) gives:

$$
\begin{aligned}
\mathbf{a_{u}}_i &= \mathbf{G_r}\mathbf{u}_i^{\mathbf{B}r} \qquad \text{and} \qquad \mathbf{b_{u}}_i = \mathbf{G_p}\mathbf{u}_i^{\mathbf{B}r} \\
\mathbf{a_{\varphi}} &= \mathbf{G_r}\boldsymbol{\varphi}^{\mathbf{B}r} \qquad \text{and} \qquad \mathbf{b_{\varphi}} = \mathbf{G_p}\boldsymbol{\varphi}^{\mathbf{B}r}
\end{aligned} \tag{43}
$$

So the interior displacement and electric potential fields have the form:

$$
\begin{aligned}
u_i^I &= [\mathbf{R}^T(\mathbf{x})\mathbf{G_r} + \mathbf{P}^T(\mathbf{x})\mathbf{G_p}]\mathbf{u}_i^{\mathbf{B}r} = \sum_{k=1}^n N_u^k(\mathbf{x})u_i^k \quad \text{in } \Omega_m \\
\varphi^I &= [\mathbf{R}^T(\mathbf{x})\mathbf{G_r} + \mathbf{P}^T(\mathbf{x})\mathbf{G_p}]\boldsymbol{\varphi}^{\mathbf{B}r} = \sum_{k=1}^n N_\varphi^k(\mathbf{x})\varphi^k \quad \text{in } \Omega_m
\end{aligned} \tag{44}
$$

In terms of nodal displacement and electric potential vectors, $\mathbf{q_u}$ and $\mathbf{q_\varphi}$, the interior displacement and electric potential fields are expressed as:

$$\mathbf{u}^I = \mathbf{N_u}(\mathbf{x})\mathbf{q_u} \quad \text{in } \Omega_m$$
$$\varphi^I = \mathbf{N_\varphi}(\mathbf{x})\mathbf{q_\varphi} \quad \text{in } \Omega_m \tag{45}$$

where $\mathbf{u}^I = \left\{ u_1^I \quad u_3^I \right\}$.

Dong and Atluri (2011) proved that for the VC-RBF to pass the patch test, when the collocation method is used, with an error reduced to a satisfactory level, the interior and boundary fields should be collocated at the quadrature points. Hence, the compatibility between internal and boundary fields is satisfied at least in a finite volume sense. For the 2D MVC-RBF, the collocation points are the Gaussian quadrature points along each boundary side (see Fig. 3), and for the 3D MVC-RBF-W, the collocation points are the 2D triangular quadrature points on the triangles generated by triangulating each polygonal surface (see Fig. 6 (right)). In this work, the collocation points used to enforce the compatibility between the interior and boundary fields are 6 (six) 1D Gaussian quadrature points on each side of the 2D MVC-RBF element, and 7 (seven) 2D triangular quadrature points, on each of the triangles generated by triangulating each polygonal surface for the 3D MVC-RBF-W element.

In principle, as the number of quadrature points increases, the error in the patch test is decreased, provided that a sufficient quadrature order is used in the integration of the stiffness matrix. However, since the integrands in the stiffness matrix are not polynomials, the numerical quadrature is always approximate, whatever the order of the quadrature. For the 2D MVC-RBF, each polygon is divided into triangles and 7 triangular quadrature points in each triangle are used in the integration of the element stiffness matrix. For the 3D MVC-RBF-W, three-dimensional Delaunay triangulation is used to divide each Voronoi Cell into a number of tetrahedrons in order to use the 3D tetrahedron numerical quadrature in calculating the stiffness matrix of each element. In this work, we use 11 quadrature points in each tetrahedron, for integrating the stiffness matrix in order to obtain sufficiently accurate results.

It should be mentioned here that the matrices that are being inverted in Eq. 39, in order to obtain $\mathbf{a_{ui}}, \mathbf{b_{ui}}, \mathbf{a_\varphi}$ and $\mathbf{b_\varphi}$, have dimensions $n \times n$, where n is the number of RBF-basis functions plus the number of the P-basis functions. Here, the number of RBF-basis functions is taken to be exactly the number of collocation points, and the RBF centers are taken to be exactly the collocation points in the whole element. Thus, n = number of collocation points + number of P-basis, which is $n = 6 \times$ number of sides of the polygon + 3 for the 2D case, and $n = 7 \times$ number of triangles on all boundaries + 4 for the 3D case.

Using the Least squares method:

When the number of collocation points is increased to a limit of infinity, it is equivalent to enforcing the compatibility between $\mathbf{u}^I$ and $\mathbf{u}^B$, and φ^I and φ^B, using the least squares method, namely minimizing the following functional:

$$e(u_i^I, u_i^B, \varphi^I, \varphi^B) = \int_{\partial\Omega_m} \left\{ (u_i^I - u_i^B)(u_i^I - u_i^B) + (\varphi^I - \varphi^B)(\varphi^I - \varphi^B) \right\} dS \qquad (46)$$

Using Eq. 31 and Eq. 34, the functional e can be written as:

$$e(\boldsymbol{\alpha}_{\mathbf{u}i}, \mathbf{q}_{\mathbf{u}i}, \boldsymbol{\alpha}_{\boldsymbol{\varphi}}, \mathbf{q}_{\boldsymbol{\varphi}}) = \int_{\partial\Omega_m} (\boldsymbol{\alpha}_{\mathbf{u}i}^T \mathbf{M}^T \mathbf{M} \boldsymbol{\alpha}_{\mathbf{u}i} - 2\boldsymbol{\alpha}_{\mathbf{u}i}^T \mathbf{M}^T \tilde{\mathbf{N}} \mathbf{q}_{\mathbf{u}i} + \mathbf{q}_{\mathbf{u}i}^T \tilde{\mathbf{N}}^T \tilde{\mathbf{N}} \mathbf{q}_{\mathbf{u}i}) dS$$
$$+ \int_{\partial\Omega_m} (\boldsymbol{\alpha}_{\boldsymbol{\varphi}}^T \mathbf{M}^T \mathbf{M} \boldsymbol{\alpha}_{\boldsymbol{\varphi}} - 2\boldsymbol{\alpha}_{\boldsymbol{\varphi}}^T \mathbf{M}^T \tilde{\mathbf{N}} \mathbf{q}_{\boldsymbol{\varphi}} + \mathbf{q}_{\boldsymbol{\varphi}}^T \tilde{\mathbf{N}}^T \tilde{\mathbf{N}} \mathbf{q}_{\boldsymbol{\varphi}}) dS \qquad (47)$$
$$= (\boldsymbol{\alpha}_{\mathbf{u}}^T \mathbf{U} \boldsymbol{\alpha}_{\mathbf{u}} - 2\boldsymbol{\alpha}_{\mathbf{u}}^T \mathbf{V} \mathbf{q}_{\mathbf{u}i} + \mathbf{q}_{\mathbf{u}i}^T \mathbf{W} \mathbf{q}_{\mathbf{u}i}) + (\boldsymbol{\alpha}_{\boldsymbol{\varphi}}^T \mathbf{U} \boldsymbol{\alpha}_{\boldsymbol{\varphi}} - 2\boldsymbol{\alpha}_{\boldsymbol{\varphi}}^T \mathbf{V} \mathbf{q}_{\boldsymbol{\varphi}} + \mathbf{q}_{\boldsymbol{\varphi}}^T \mathbf{W} \mathbf{q}_{\boldsymbol{\varphi}})$$

To minimize e for a fixed $\mathbf{q}_{\mathbf{u}i}$ and $\mathbf{q}_{\boldsymbol{\varphi}}$ we have,

$$\delta e(\delta\boldsymbol{\alpha}_{\mathbf{u}i}, \mathbf{q}_{\mathbf{u}i}, \delta\boldsymbol{\alpha}_{\boldsymbol{\varphi}}, \mathbf{q}_{\boldsymbol{\varphi}}) =$$
$$(2\delta\boldsymbol{\alpha}_{\mathbf{u}}^T \mathbf{U} \boldsymbol{\alpha}_{\mathbf{u}} - 2\delta\boldsymbol{\alpha}_{\mathbf{u}}^T \mathbf{V} \mathbf{q}_{\mathbf{u}i}) + (2\delta\boldsymbol{\alpha}_{\boldsymbol{\varphi}}^T \mathbf{U} \boldsymbol{\alpha}_{\boldsymbol{\varphi}} - 2\delta\boldsymbol{\alpha}_{\boldsymbol{\varphi}}^T \mathbf{V} \mathbf{q}_{\boldsymbol{\varphi}}) \qquad (48)$$

This should be true for any $\delta\boldsymbol{\alpha}_{\mathbf{u}i}$ and $\delta\boldsymbol{\alpha}_{\boldsymbol{\varphi}}$, hence;

$$\mathbf{U}\boldsymbol{\alpha}_{\mathbf{u}i} = \mathbf{V}\mathbf{q}_{\mathbf{u}i}, \quad \text{or} \quad \boldsymbol{\alpha}_{\mathbf{u}i} = \mathbf{L}_{\mathbf{u}}\mathbf{q}_{\mathbf{u}i}$$
$$\mathbf{U}\boldsymbol{\alpha}_{\boldsymbol{\varphi}} = \mathbf{V}\mathbf{q}_{\boldsymbol{\varphi}}, \quad \text{or} \quad \boldsymbol{\alpha}_{\boldsymbol{\varphi}} = \mathbf{L}_{\boldsymbol{\varphi}}\mathbf{q}_{\boldsymbol{\varphi}} \qquad (49)$$

Substituting this into the second equation in Eq. 31 gives:

$$u_i^I = \mathbf{M}(\mathbf{x})\boldsymbol{\alpha}_{\mathbf{u}i} = \mathbf{M}(\mathbf{x})\mathbf{L}_{\mathbf{u}}\mathbf{q}_{\mathbf{u}i} \quad \text{or} \quad \mathbf{u}^I = \mathbf{N}_{\mathbf{u}}(\mathbf{x})\mathbf{q}_{\mathbf{u}} \quad \text{in } \Omega_m$$
$$\varphi^I = \mathbf{M}(\mathbf{x})\boldsymbol{\alpha}_{\boldsymbol{\varphi}} = \mathbf{M}(\mathbf{x})\mathbf{L}_{\boldsymbol{\varphi}}\mathbf{q}_{\boldsymbol{\varphi}} = \mathbf{N}_{\boldsymbol{\varphi}}(\mathbf{x})\mathbf{q}_{\boldsymbol{\varphi}} \quad \text{in } \Omega_m \qquad (50)$$

Only the square matrix $\mathbf{U} = \int_{\partial\Omega_m} \mathbf{M}^T \mathbf{M} dS$ is being inverted here. The dimensions of this matrix is also $n \times n$ where n is the number of RBF-basis functions plus the number of the P-basis functions. If we take the number of RBF-basis to be exactly the same as that of the integration points in the whole element as we did in the case of the collocation method, the number of unknowns $\boldsymbol{\alpha}_{\mathbf{u}i} = \begin{Bmatrix} \mathbf{a}_{\mathbf{u}i} \\ \mathbf{b}_{\mathbf{u}i} \end{Bmatrix}$ or $\boldsymbol{\alpha}_{\boldsymbol{\varphi}} = \begin{Bmatrix} \mathbf{a}_{\boldsymbol{\varphi}} \\ \mathbf{b}_{\boldsymbol{\varphi}} \end{Bmatrix}$ will be larger than that of the equations (in a collocation sense) by the number of the P-basis functions (3 for 2D element and 4 for 3D element). So the number of integration points in the whole element used in evaluating $\mathbf{U}$ and $\mathbf{V}$ matrices should

be larger than that of the RBF basis functions.

For the 3D MVC-RBF-W, we selected the RBF centers to be at the 3 (three) Gaussian points in each triangle of the triangulated boundary surfaces, while 7 (seven) Gaussian points per triangle are used in integration. Hence the number of RBF basis functions is $3 \times$ number of triangles on all boundaries. This number of RBF basis functions proved to be enough to give sufficient accuracy of the element unlike the case of the collocation method where 7 collocation points per triangle are required to give an acceptable accuracy. Thus, $n = 3 \times$ number of triangles on all boundaries $+ 4$. This number n is much less than that used in the collocation method, and hence the least square method yields a much cheaper element while also leading to better accuracy as was illustrated in [Bishay and Atluri (2012)].

3.2   *Finite element equation*

Having the interior fields in terms of the nodal values of mechanical displacements and electric potential (as in Eq. 45 for the collocation method, and Eq. 50 for the least square method), the corresponding interior strain and electric field intensity are:

$$\boldsymbol{\varepsilon}^I = \boldsymbol{\partial_u u}^I = \boldsymbol{\partial_u}(\mathbf{N_u}(\xi^\gamma)\mathbf{q_u}) = \mathbf{B_u}(\mathbf{x})\mathbf{q_u} \quad \text{in } \Omega_m$$
$$-\mathbf{E}^I = \boldsymbol{\partial_e}\varphi^I = \boldsymbol{\partial_e}(\mathbf{N_\varphi}(\xi^\gamma)\mathbf{q_\varphi}) = \mathbf{B_\varphi}(\mathbf{x})\mathbf{q_\varphi} \quad \text{in } \Omega_m$$

(51)

Now we can use $\Pi(\mathbf{u}, \varphi)$, a functional used for developing irreducible or primal finite elements [Sze and Pan (1999)], to obtain the finite element equation for any of the two mentioned methods:

$$\Pi(\mathbf{u}, \varphi) = \int_\Omega \left[\frac{1}{2} \left\{ \begin{matrix} \boldsymbol{\partial_u u} \\ \boldsymbol{\partial_e \varphi} \end{matrix} \right\}^T \begin{bmatrix} \mathbf{C} & \mathbf{e}^T \\ \mathbf{e} & -\mathbf{h} \end{bmatrix} \left\{ \begin{matrix} \boldsymbol{\partial_u u} \\ \boldsymbol{\partial_e \varphi} \end{matrix} \right\} - \overline{\mathbf{b}}^T \mathbf{u} + \overline{\rho_f}\varphi \right] d\Omega$$
$$- \int_{S_t} \overline{\mathbf{t}}^T \mathbf{u} dS - \int_{S_Q} \overline{Q}\varphi dS$$

(52)

Substituting the finite element interpolation functions, Eq. 45 and Eq. 51, we get after dropping the superscript I for simplicity and considering that the body is composed of N finite elements ($\Omega = \sum_{k=1}^N \Omega_k$):

$$\Pi = \sum_{k=1}^N \left(\begin{matrix} \frac{1}{2} \left\{ \begin{matrix} \mathbf{q_u^k} \\ \mathbf{q_\varphi^k} \end{matrix} \right\}^T \begin{bmatrix} \int_{\Omega_k} \mathbf{B_u^T C^k B_u} d\Omega & \int_{\Omega_k} \mathbf{B_u^T e^{kT} B_\varphi} d\Omega \\ \int_{\Omega_k} \mathbf{B_\varphi^T e^k B_u} d\Omega & -\int_{\Omega_k} \mathbf{B_\varphi^T h^k B_\varphi} d\Omega \end{bmatrix} \left\{ \begin{matrix} \mathbf{q_u^k} \\ \mathbf{q_\varphi^k} \end{matrix} \right\} \\ - \left(\int_{\Omega_k} \overline{\mathbf{b}}^{kT} \mathbf{N_u} d\Omega \right) \mathbf{q_u^k} + \left(\int_{\Omega_k} \overline{\rho}_f^k \mathbf{N_\varphi} d\Omega \right) \mathbf{q_\varphi^k} \\ - \left(\int_{S_t^k} \overline{\mathbf{t}}^{kT} \mathbf{N_u} dS \right) \mathbf{q_u^k} - \left(\int_{S_Q^k} \overline{Q}^k \mathbf{N_\varphi} dS \right) \mathbf{q_\varphi^k} \end{matrix} \right)$$

(53)

Equating the first variation of this functional with respect to $\left\{ \mathbf{q_u^k} \quad \mathbf{q_\varphi^k} \right\}^T$ to zero, leads to the global finite element equation that is solved for the global nodal primal variables $\mathbf{q} = \left\{ \mathbf{q_u} \quad \mathbf{q_\varphi} \right\}^T = \sum_{k=1}^{N} \left\{ \mathbf{q_u^k} \quad \mathbf{q_\varphi^k} \right\}^T$:

$$\mathbf{Kq} = \mathbf{F} \tag{54}$$

with the stiffness matrix and load vector having, respectively, the forms:

$$\mathbf{K} = \sum_{k=1}^{N} \begin{bmatrix} \int_{\Omega_k} \mathbf{B_u}^T \mathbf{C}^k \mathbf{B_u} d\Omega & \int_{\Omega_k} \mathbf{B_u}^T \mathbf{e}^{kT} \mathbf{B_\varphi} d\Omega \\ \int_{\Omega_k} \mathbf{B_\varphi}^T \mathbf{e}^k \mathbf{B_u} d\Omega & -\int_{\Omega_k} \mathbf{B_\varphi}^T \mathbf{h}^k \mathbf{B_\varphi} d\Omega \end{bmatrix} \tag{55}$$

$$\mathbf{F} = \begin{Bmatrix} \mathbf{F_u} \\ \mathbf{F_\varphi} \end{Bmatrix} = \begin{Bmatrix} \int_{\Omega_k} \overline{\mathbf{b}}^{kT} \mathbf{N_u} d\Omega + \int_{S_t^k} \overline{\mathbf{t}}^{kT} \mathbf{N_u} dS \\ -\int_{\Omega_k} \overline{\rho}_f^k \mathbf{N_\varphi} d\Omega + \int_{S_Q^k} \overline{Q}^k \mathbf{N_\varphi} dS \end{Bmatrix} \tag{56}$$

We denote the 2D version of this element as "MVC-RBF-1" while the 3D version as "MVC-RBF-W-1".

By increasing the number of RBF center/collocation points, the residual error produced in the patch test can be reduced to a satisfactory level. However, MVC-RBF1 and MVC-RBF-W-1 may suffer from locking because the assumed interior displacement field is only complete to the first order, and the derived strains are locked together. This not only affects the accuracy of the mechanical displacements but also affect that of the electric potential due to the piezoelectric coupling. To improve the performance of MVC-RBF-1 and MVC-RBF-W-1, we can further independently assume an interior strain field $\varepsilon_{ij}^{In}(\mathbf{x}, \boldsymbol{\alpha})$ which eliminates the shear locking terms, and determine the undetermined parameters $\boldsymbol{\alpha}$ by enforcing the compatibility between $\varepsilon_{ij}^{In}(\mathbf{x}, \boldsymbol{\alpha})$ and $\varepsilon_{ij}^I(\mathbf{x}, \mathbf{q_u})$ at several preselected collocation points. Similarly we can assume independent electric field $E_i^{In}(\mathbf{x}, \boldsymbol{\beta})$ and collocate it with the electric field derived from the electric potential $E_i^I(\mathbf{x}, \mathbf{q_\varphi})$;

For the 2D element:

$$\begin{aligned} \varepsilon_1^{In} &= \mathbf{A_{\varepsilon 1}}(\xi^\gamma) \boldsymbol{\alpha_I}, \quad \varepsilon_3^{In} = \mathbf{A_{\varepsilon 3}}(\xi^\gamma) \boldsymbol{\alpha_{II}}, \quad \varepsilon_5^{In} = \mathbf{A_{\varepsilon 5}}(\xi^\gamma) \boldsymbol{\alpha_{III}}, \\ -E_1^{In} &= \mathbf{A_{E1}}(\xi^\gamma) \boldsymbol{\beta_I}, \quad -E_3^{In} = \mathbf{A_{E3}}(\xi^\gamma) \boldsymbol{\beta_{II}} \end{aligned} \tag{57}$$

and for the 3D element:

$$\begin{aligned} \varepsilon_1^{In} &= \mathbf{A_{\varepsilon 1}}(\xi^\gamma) \boldsymbol{\alpha_I}, \quad \varepsilon_2^{In} = \mathbf{A_{\varepsilon 2}}(\xi^\gamma) \boldsymbol{\alpha_{II}}, \quad \varepsilon_3^{In} = \mathbf{A_{\varepsilon 3}}(\xi^\gamma) \boldsymbol{\alpha_{III}}, \\ \varepsilon_4^{In} &= \mathbf{A_{\varepsilon 4}}(\xi^\gamma) \boldsymbol{\alpha_{IV}}, \quad \varepsilon_5^{In} = \mathbf{A_{\varepsilon 5}}(\xi^\gamma) \boldsymbol{\alpha_V}, \quad \varepsilon_6^{In} = \mathbf{A_{\varepsilon 6}}(\xi^\gamma) \boldsymbol{\alpha_{VI}}, \\ -E_1^{In} &= \mathbf{A_{E1}}(\xi^\gamma) \boldsymbol{\beta_I}, \quad -E_2^{In} = \mathbf{A_{E2}}(\xi^\gamma) \boldsymbol{\beta_{II}}, \quad -E_3^{In} = \mathbf{A_{E3}}(\xi^\gamma) \boldsymbol{\beta_{III}} \end{aligned} \tag{58}$$

Collocating the independent fields (the components of normal strains and electric field) in Eq. 57 or Eq. 58 with that of equation Eq. 51 at enough points inside the

element, and collocating the shear terms (ε_5^{In} for the 2D case and ε_4^{In}, ε_5^{In} and ε_6^{In} for the 3D case) only at the center of the element, we get:

$$
\begin{aligned}
\boldsymbol{\varepsilon}^{In} &= \mathbf{A}_{\boldsymbol{\varepsilon}}(\xi^\gamma)\boldsymbol{\alpha} = \mathbf{B}_{\mathbf{u}}^*(\xi^\gamma)\mathbf{q_u}, \\
\mathbf{E}^{In} &= \mathbf{A}_{\mathbf{E}}(\xi^\gamma)\boldsymbol{\beta} = \mathbf{B}_{\boldsymbol{\varphi}}^*(\xi^\gamma)\mathbf{q_\varphi},
\end{aligned}
\tag{59}
$$

Then we substitute in the functional Π as was done in Eq. 53 to get the stiffness matrix and load vector as similar to that in Eq. 55 and Eq. 56, respectively, but with replacing $\mathbf{B}_{\mathbf{u}}(\xi^\gamma)$ and $\mathbf{B}_{\boldsymbol{\varphi}}(\xi^\gamma)$ with $\mathbf{B}_{\mathbf{u}}^*(\xi^\gamma)$ and $\mathbf{B}_{\boldsymbol{\varphi}}^*(\xi^\gamma)$. We denote the 2D version of this element by "MVC-RBF-2" and the 3D version as "MVC-RBF-W-2". Actually the stiffness matrix of MVC-RBF-2 and MVC-RBF-W-2 can be derived using the same procedure of deriving MVC-RBF-1 and MVC-RBF-W-1, only by substituting the center point at every quadrature point in integrating the shear strains.

3.3 Conditioning of the system matrices

The finite element global system of equations to be solved in any of the previously presented elements is ill-conditioned because the stiffness matrix contains the material elastic stiffness matrix $\mathbf{C}$ in the $\mathbf{K_{uu}}$ part and also contains the dielectric material matrix $\mathbf{h}$ in the $\mathbf{K_{\varphi\varphi}}$ part. The numerical values of the components of $\mathbf{C}$ are as large as 10^{10}, and that of $\mathbf{h}$ are as small as 10^{-9}. Hence the ratio is as large as 10^{19}, and this makes the global stiffness matrix ill-conditioned. To improve the conditioning we can use the following matrix instead of that of Eq. 11:

$$
\begin{Bmatrix} \hat{\boldsymbol{\sigma}} \\ \hat{\mathbf{D}} \end{Bmatrix} = \begin{bmatrix} \hat{\mathbf{C}} & \hat{\mathbf{e}}^T \\ \hat{\mathbf{e}} & -\hat{\mathbf{h}} \end{bmatrix} \begin{Bmatrix} \boldsymbol{\varepsilon} - \boldsymbol{\varepsilon}^{\mathbf{R}} \\ -\hat{\mathbf{E}} \end{Bmatrix} + \begin{Bmatrix} \mathbf{0} \\ \hat{\mathbf{P}}^{\mathbf{R}} \end{Bmatrix}
\tag{60}
$$

where

$$
\hat{\sigma}_i = \frac{\sigma_i}{\tilde{c}}, \quad \hat{D}_i = \frac{D_i}{\tilde{e}}, \quad \hat{E}_i = \frac{E_i\tilde{e}}{\tilde{c}}, \quad \hat{P}_i^R = \frac{P_i^R}{\tilde{e}}
$$

and

$$
\hat{C}_{ij} = \frac{C_{ij}}{\tilde{c}}, \quad \hat{e}_{ij} = \frac{e_{ij}}{\tilde{e}}, \quad \hat{h}_{ij} = \frac{h_{ij}\tilde{c}}{\tilde{e}^2}.
$$

and from Eq. 4, we also have $\hat{\varphi} = \frac{\varphi\tilde{e}}{\tilde{c}}$.
Here we can select $\tilde{c} = C_{11}$ and $\tilde{e} = e_{33}$.
Hence, the stiffness matrix will have the form:

$$
\hat{\mathbf{K}} = \begin{bmatrix} \hat{\mathbf{K}}_{\mathbf{uu}} & \hat{\mathbf{K}}_{\mathbf{u\varphi}} \\ \hat{\mathbf{K}}_{\mathbf{u\varphi}}^T & -\hat{\mathbf{K}}_{\boldsymbol{\varphi\varphi}} \end{bmatrix} = \sum_{k=1}^{N} \begin{bmatrix} \int_{\Omega_k} \mathbf{B}_{\mathbf{u}}^T \hat{\mathbf{C}}^k \mathbf{B}_{\mathbf{u}} d\Omega & \int_{\Omega_k} \mathbf{B}_{\mathbf{u}}^T \hat{\mathbf{e}}^{kT} \mathbf{B}_{\boldsymbol{\varphi}} d\Omega \\ \int_{\Omega_k} \mathbf{B}_{\boldsymbol{\varphi}}^T \hat{\mathbf{e}}^k \mathbf{B}_{\mathbf{u}} d\Omega & -\int_{\Omega_k} \mathbf{B}_{\boldsymbol{\varphi}}^T \hat{\mathbf{h}}^k \mathbf{B}_{\boldsymbol{\varphi}} d\Omega \end{bmatrix}
\tag{61}
$$

and the system to be solved will be:

$$\hat{\mathbf{K}}\hat{\mathbf{q}} = \hat{\mathbf{F}} \tag{62}$$

Where

$$\hat{\mathbf{F}} = \left\{ \begin{matrix} \hat{\mathbf{F}}_\mathbf{u} \\ \hat{\mathbf{F}}_{\boldsymbol{\varphi}} \end{matrix} \right\}, \quad \hat{\mathbf{F}}_\mathbf{u} = \frac{\mathbf{F}_\mathbf{u}}{\tilde{c}}, \quad \hat{\mathbf{F}}_{\boldsymbol{\varphi}} = \frac{\mathbf{F}_{\boldsymbol{\varphi}}}{\tilde{e}}$$

$$\hat{\mathbf{q}} = \left\{ \mathbf{q}_\mathbf{u} \quad \hat{\mathbf{q}}_{\boldsymbol{\varphi}} \right\}^T \quad \text{and} \quad \hat{\mathbf{q}}_{\boldsymbol{\varphi}} = \frac{\mathbf{q}_{\boldsymbol{\varphi}}\tilde{e}}{\tilde{c}}. \tag{63}$$

So, we solve the system (62) for $\mathbf{q}$ from which we get $\mathbf{q}_\mathbf{u}$ and $\mathbf{q}_{\boldsymbol{\varphi}} = \frac{\hat{\mathbf{q}}_{\boldsymbol{\varphi}}\tilde{c}}{\tilde{e}}$.

4   Switching criterion and kinetics

Gibbs energy density g can be related to the internal energy density U via a Legendre transformation, which results in:

$$\rho g = \rho U - \boldsymbol{\sigma} : \boldsymbol{\varepsilon} - \mathbf{E} \cdot \mathbf{D} - \eta T \tag{64}$$

Gibbs energy is considered to be composed of two parts, a linear (or reversible) part, g^L , which reflects the linear or reversible responses of the material and primarily depends on $\boldsymbol{\sigma}$, $\mathbf{E}$ and T , and a remnant (or irreversible) part, g^R , arising from the changes in the remnant state of the crystal with respect to a reference state, and is assumed to be a function of the remnant polarization and strain.

$$g = g^L(\boldsymbol{\sigma}, \mathbf{E}, T) + g^R(\mathbf{P}^\mathbf{R}, \boldsymbol{\varepsilon}^\mathbf{R}) \tag{65}$$

Substituting Eq. 8, Eq. 13, Eq. 64 and Eq. 65 into Eq. 14, we get the local dissipation inequality for the isothermal case considered :

$$\boldsymbol{\sigma} : \dot{\boldsymbol{\varepsilon}}^\mathbf{R} + \mathbf{E} \cdot \dot{\mathbf{P}}^\mathbf{R} - \rho \partial_{\boldsymbol{\varepsilon}^\mathbf{R}} g^R \cdot \dot{\boldsymbol{\varepsilon}}^\mathbf{R} - \rho \partial_{\mathbf{P}^\mathbf{R}} g^R \cdot \dot{\mathbf{P}}^\mathbf{R} \geq 0 \tag{66}$$

In the case of a reversible response, the microscopic state of the crystal, as well as the remnant values, remain unaltered-such that $\dot{\mathbf{P}}^\mathbf{R} = \mathbf{0}$ and $\dot{\boldsymbol{\varepsilon}}^\mathbf{R} = \mathbf{0}$, and Eq. 66 turns into an equality taking the value zero. In this work, rate-effects will not be accounted for and also changes in volume fractions are done at discrete time intervals $\Delta t > 0$.

Several representation forms of the Gibbs energy associated with the remnant state of the crystal, $g^R(\mathbf{P}^\mathbf{R}, \boldsymbol{\varepsilon}^\mathbf{R})$, have been investigated in the literature (see Cooks and McMeeking (1999) and Kamlah and Jinag (1999) for example). Here we restrict

ourselves to a quadratic form in terms of the remnant polarization and strains, namely:

$$\rho g^R(\mathbf{P^R}, \boldsymbol{\varepsilon^R}) = \frac{1}{2} \boldsymbol{\varepsilon^R} : \mathbf{H}_{\boldsymbol{\varepsilon}} : \boldsymbol{\varepsilon^R} + \frac{1}{2} \mathbf{P^R} \cdot \mathbf{H_P} \cdot \mathbf{P^R} \tag{67}$$

Where $\mathbf{H}_{\boldsymbol{\varepsilon}}$ and $\mathbf{H_P}$ denote the hardening-type tensors pertaining to the crystal's remnant strain and polarization respectively. Here, we assume the simplest format, i.e. the hardening-type tensors are chosen to be proportional to the symmetric identity tensors of fourth and second order:

$$\mathbf{H}_{\boldsymbol{\varepsilon}} = H_{\varepsilon} \mathbf{I}^{sym}, \quad \mathbf{H_P} = H_P \mathbf{I}^{sym} \tag{68}$$

Where H_{ε} and H_P are positive scalars, being referred to as hardening parameters, $\mathbf{I}^{sym}$ is a symmetric identity tensor of the fourth order for strain and second order for polarization. H_{ε} and H_P are set constant in this work. Based on Eq. 66 and Eq. 67, the local dissipation inequality now corresponds to

$$\left[\boldsymbol{\sigma} - \boldsymbol{\sigma^b} \right] : \dot{\boldsymbol{\varepsilon}}^{\mathbf{R}} + \left[\mathbf{E} - \mathbf{E^b} \right] \cdot \dot{\mathbf{P}}^{\mathbf{R}} \geq 0 \tag{69}$$

With

$$\boldsymbol{\sigma^b} = \rho \partial_{\boldsymbol{\varepsilon^R}} g^R = \mathbf{H}_{\boldsymbol{\varepsilon}} : \boldsymbol{\varepsilon^R} = H_{\varepsilon} \boldsymbol{\varepsilon^R} \tag{70}$$

$$\mathbf{E^b} = \rho \partial_{\mathbf{P^R}} g^R = \mathbf{H_P} \cdot \mathbf{P^R} = H_P \mathbf{P^R} \tag{71}$$

The contributions $\boldsymbol{\sigma^b}$ and $\mathbf{E^b}$ are referred to as back stresses and back electric field, respectively. If the remnant polarization and strain of a grain vary from a reference state, the back fields will either resist or assist further domain switching processes depending upon whether the process will take the current state further away from the reference state or closer to it. Here, the reference state is defined as the state at which the remnant polarization and strain of the single grain are zero.

The rate of change of the remnant strain and polarization is calculated from Eq. 9 as:

$$\dot{\boldsymbol{\varepsilon}}^{\mathbf{R}} = \sum_{i=1}^{N_d} \dot{c}_i \boldsymbol{\varepsilon}_i^{\mathbf{S}}, \quad \dot{\mathbf{P}}^{\mathbf{R}} = \sum_{i=1}^{N_d} \dot{c}_i \mathbf{P}_i^{\mathbf{S}} \tag{72}$$

Substitution of Eq. 72 into Eq. 69 yields the local dissipation inequality to result in:

$$\sum_{i=1}^{N_d} \left[\left[\boldsymbol{\sigma} - \boldsymbol{\sigma^b} \right] : \boldsymbol{\varepsilon}_i^{\mathbf{S}} + \left[\mathbf{E} - \mathbf{E^b} \right] \cdot \mathbf{P}_i^{\mathbf{S}} \right] \dot{c}_i \geq 0 \quad \text{or} \quad \sum_{i=1}^{N_d} f_i \dot{c}_i \geq 0 \tag{73}$$

At the level of a single crystal, f_i denotes the force driving domain switching processes by altering the crystal variant i in combination with one or more of the remaining variants.

The switching criterion specifies the conditions under which domain switching commences. Let a domain switching process-transforming one variant into another-be referred to as a transformation system. For a 2D ferroelectric body with four types of different phases per element or grain, 6 such transformation systems can be observed, while for the 3D case with six types of variants, we have 15 transformation systems.

Concerning notation, a transformation system that increases the variant j at the expense of another variant, say i, is denoted as $i \rightarrow j$. The related driving force f_{ij} is obtained from Eq. 73 as,

$$f_{ij} = f_j - f_i = \left[\boldsymbol{\sigma} - \boldsymbol{\sigma^b}\right] : \boldsymbol{\varepsilon}^{\mathbf{S}}_{i \rightarrow j} + \left[\mathbf{E} - \mathbf{E^b}\right] \cdot \mathbf{P}^{\mathbf{S}}_{i \rightarrow j} \quad \text{for } i, j = 1..N_d \tag{74}$$

Where $\boldsymbol{\varepsilon}^{\mathbf{S}}_{i \rightarrow j} = \boldsymbol{\varepsilon}^{\mathbf{S}}_j - \boldsymbol{\varepsilon}^{\mathbf{S}}_i$ and $\mathbf{P}^{\mathbf{S}}_{i \rightarrow j} = \mathbf{P}^{\mathbf{S}}_j - \mathbf{P}^{\mathbf{S}}_i$.

For the 2D case, four of the six possible forward transformation systems are related to 90° domain switching, while the remaining two correspond to 180° domain switching. For the 3D case, 12 of the possible 15 forward transformation systems are related to 90° domain switching, while the remaining three correspond to 180° domain switching. Once the driving force reaches a certain critical threshold values k_{90} or k_{180} associated with 90° or 180° domain switching respectively, the modeling of the related switching process is initiated. In other words, the transformation system is activated based on:

$$\begin{aligned} |f_{ij}| \geq k_{90} \quad &\Rightarrow 90° \text{ switching} \\ |f_{ij}| \geq k_{180} \quad &\Rightarrow 180° \text{ switching} \end{aligned} \tag{75}$$

So, the ferroelectric crystal exhibits reversible responses without any change in its microscopic state because the underlying volume fractions of crystal variants are unaltered until the driving force reaches any of the critical values. Once a transformation system becomes active, the associated discrete changes in the volume fractions as referred to the time or rather load interval $\Delta t > 0$ can be determined using Eq. 74 and Eq. 75. The update of a crystal variant j according to the $i \rightarrow j$ transformation system is represented by

$$\Delta c_j = \begin{cases} -\min\{c_i, \Delta \tilde{c}_j\}, & \text{for } f_{ij} \leq -f_{cr} \\ 0, & \text{for } -f_{cr} \leq f_{ij} \leq f_{cr} \\ \min\{c_i, \Delta \tilde{c}_j\}, & \text{for } f_{ij} \geq f_{cr} \end{cases} \tag{76}$$

Where

$$f_{cr} = \begin{cases} k_{90}, & \text{for } 90° \text{ switching} \\ k_{180}, & \text{for } 180° \text{ switching} \end{cases}$$

and

$$\Delta \tilde{c}_j = \frac{\langle |f_{ij}| - f_{cr} \rangle}{\boldsymbol{\varepsilon}^{\mathbf{S}}_{i \to j} : \mathbf{H}_{\boldsymbol{\varepsilon}} : \boldsymbol{\varepsilon}^{\mathbf{S}}_{i \to j} + \mathbf{P}^{\mathbf{S}}_{i \to j} : \mathbf{H}_{\mathbf{P}} : \mathbf{P}^{\mathbf{S}}_{i \to j}} \tag{77}$$

Where $\langle \bullet \rangle = \frac{1}{2}[| \bullet | + \bullet]$. Note that:

$$\boldsymbol{\varepsilon}^{\mathbf{S}}_1 = \boldsymbol{\varepsilon}^{\mathbf{S}}_2, \ \boldsymbol{\varepsilon}^{\mathbf{S}}_3 = \boldsymbol{\varepsilon}^{\mathbf{S}}_4, \text{ and } \boldsymbol{\varepsilon}^{\mathbf{S}}_5 = \boldsymbol{\varepsilon}^{\mathbf{S}}_6$$
$$\mathbf{P}^{\mathbf{S}}_1 = -\mathbf{P}^{\mathbf{S}}_2, \ \mathbf{P}^{\mathbf{S}}_3 = -\mathbf{P}^{\mathbf{S}}_4, \text{ and } \mathbf{P}^{\mathbf{S}}_5 = -\mathbf{P}^{\mathbf{S}}_6$$

Hence for 180° switching, there is no change in the remnant strain and Eq. 77 reduces to:

$$\Delta \tilde{c}_j = \frac{\langle |f_{ij}| - k_{180} \rangle}{4 \mathbf{P}^{\mathbf{S}}_j : \mathbf{H}_{\mathbf{P}} : \mathbf{P}^{\mathbf{S}}_j}$$

Note that the consistency constraints on the volume fractions (see Eq. 7) are inherently guaranteed within the proposed model as the relation $f_{ij} = -f_{ji}$ generally holds. So for the forward transformation system $i \to j$ the volume fraction c_j increases by the same amount as c_i decreases. Once the incremental volume fractions are obtained, the volume fractions of each element should be updated:

$$c_{j(new)} = c_{j(old)} + \sum_{i=1, i \neq j}^{N_d} \Delta c_{ij} \quad \text{for } j = 1..N_d \tag{78}$$

Then, the material matrices as well as the remnant strain and polarization can be updated using Eq. 9, while the back fields of the current crystal state can be determined via Eq. 70 and Eq. 71. As the back fields resist subsequent switching process in the same transformation system, increasing loading levels are required to continue the transformation of the respective phase. If the loading direction is reversed, however, the back fields additionally support the transformation process until the crystal reaches the reference state. Hardening or softening effects within the crystal- stemming from changing remnant states-are accounted for in the model by means of these back fields. In order to realize the crystal-to-crystal interactions in a ferroelectric polycrystal, i.e. the so-called intergranular effects, as well as to simulate general boundary value problems, the single crystal model proposed is

embedded into an iterative finite element framework as will be discussed in the next section.

Note that the switching criterion used here is local in nature, unlike the switching criterion of [Kim and Jiang (2002) and others] which is based on the overall energy release of the whole body. Using this local switching criterion prevents searching for the configuration that yields the minimum overall energy of the whole body in each simulation step. This search for the desired configuration requires solving the finite element system of equations as much as the number of the switching elements (the elements that tend to switch) in each simulation step. Hence it is computationally inefficient.

5 Solution method

To calculate the response of a polycrystalline ferroelectric under electromechanical loading, the switching criterion and kinetic relations presented in the previous section should be implemented into a numerical algorithm to obtain the volume fractions of various domains in each grain at each time step. First the body is discretized to randomly generated Voronoi Cells (MVCs). Each MVC represents one crystal grain. Then randomly generated crystallographic axes are assigned to each MVC, modeling a crystal grain in a polycrystalline ferroelectric specimen. This is done by generating a random value for the angle θ -between the global X_1 axis and the local crystal axis 1, x'_1 , in each element for the 2D analysis. x'_3 or the crystal axis 3 is set by a 90° rotation of x'_1 , in the $X_1 - X_3$ plane. For the 3D case, three Euler angles (θ, ϕ and ψ) are generated randomly for each polyhedron element to define its crystallographic axes as was discussed in subsection 2.1. The crystallographic axes are mutually orthogonal.

Initially, each MVC modeling a crystal grain consists of N_d distinct types of domains, where N_d is the number of possible domain types in the element ($N_d = 4$ in the 2D analysis and $N_d = 6$ for the 3D case). The spontaneous polarization directions of the domains are parallel/opposite to the crystallographic axes in each element. Hence for the system configuration which is defined by domain volume fractions, all the element domains are assigned with the same initial values of volume fraction, i.e. $1/N_d$. The net polarization and strain of the specimen are therefore zero at the initial instant of time. The back fields are also zero initially.

Suppose that the system configuration at time t is known. After an incremental time step Δt, the system configuration at time $t + \Delta t$ are determined as follows:

(a) The load vector $\mathbf{F}$ is updated to that at time $t + \Delta t$. By using the known values of volume fractions at time t and the known load vector at time $t + \Delta t$, the finite element system of equation is assembled and solved to obtain a new nodal electromechanical displacements $\mathbf{q} = \left\{ \mathbf{q_u} \quad \mathbf{q_\varphi} \right\}^T$. Based on the new element elec-

tromechanical displacement vector $\mathbf{q}$, the element area (volume) average linear strain and electric field are calculated as:

$$\bar{\boldsymbol{\varepsilon}}^{\mathbf{L}k} = \frac{\int_{A^k} \boldsymbol{\varepsilon}^{\mathbf{L}} dA}{A^k} = \frac{\int_{A^k} \mathbf{B_u} dA}{A^k} \mathbf{q_u} \tag{79}$$

$$\bar{\mathbf{E}}^k = \frac{\int_{A^k} \mathbf{E} dA}{A^k} = \frac{-\int_{A^k} \mathbf{B_\varphi} dA}{A^k} \mathbf{q_\varphi} \tag{80}$$

Where A and A^k are replaced by V and V^k respectively for the 3D case. A^k and V^k are the area and volume of element k respectively.

Then the element area (volume) average stress $\bar{\boldsymbol{\sigma}}^k$ and linear electric displacement $\bar{\mathbf{D}}^{kL}$ are calculated from the linear constitutive relations (Eq. 12) in which the material matrices are determined with the known values of volume fractions at time t.

$$\begin{Bmatrix} \bar{\boldsymbol{\sigma}}^k \\ \bar{\mathbf{D}}^{\mathbf{L}k} \end{Bmatrix} = \begin{bmatrix} \mathbf{C}^k & \mathbf{e}^{kT} \\ \mathbf{e}^k & -\mathbf{h}^k \end{bmatrix} \begin{Bmatrix} \bar{\boldsymbol{\varepsilon}}^{\mathbf{L}k} \\ -\bar{\mathbf{E}}^k \end{Bmatrix} \tag{81}$$

(b) All the domains in an element are assumed to be subjected to constant electric field and stress, $\bar{\mathbf{E}}$ and $\bar{\boldsymbol{\sigma}}$. The driving force for all the transformation systems, f_{ij} , in each element can then be computed using Eq. 74, and compared with the critical values k_{90} and k_{180} . If driving forces are less than the critical values, then no switching is done and loading is continued elastically.

(c) Once the driving force of any transformation system in an element exceeds the corresponding critical value, then increments in the volume fractions can be calculated using Eq. 76 and the volume fractions of all the domains in each element can be updated using Eq. 78. The average material matrices, remnant strain, $\boldsymbol{\varepsilon}^{\mathbf{R}k}$, and polarization, $\mathbf{P}^{\mathbf{R}k}$, as well as the back fields in each element should also be updated using Eq. 9, Eq. 70 and Eq. 71. Then the element's macroscopic strain and polarization are calculated using Eq. 8.

(d) Using the new average material properties, the system of equations is assembled and solved. A new set of nodal electromechanical displacements can be obtained. For the same simulation step or load increment, the previous steps should be repeated with the new/updated volume fractions until some convergence criterion is met.

By repeating the steps (a)-(d), the system configuration at the next time step can be found.

It was shown in [Jayabal et al. (2011)], that for sufficiently small load increments further iteration steps for the local volume fractions at fixed external loads (as described in (d)) are not necessary and do not significantly change the solution of the

boundary value problems investigated. Moreover, by not allowing for additional iteration steps for a given load increment, the possible problem of back and forth switching, which depends in particular on the orientation of the local crystallographic axes with respect to the loading directions, is avoided. This algorithmic problem is due to the discrete nature of the switching criterion introduced.

6   Results

In this section, we present the results of the developed MVC-RBF models for ferroelectric switching (by applying cyclic electric loads that may be combined with constant mechanical loads) and ferroelastic switching (by applying only cyclic mechanical loads). The material used for the simulation is $BaTiO_3$. The properties of a $BaTiO_3$ crystal poled in x'_3- crystallographic axis are:

$C_{11} = 16.6 \times 10^{10}$, $C_{12} = 7.7 \times 10^{10}$, $C_{13} = 7.75 \times 10^{10}$, $C_{33} = 16.2 \times 10^{10}$
$C_{44} = 4.29 \times 10^{10}$ N/m^2; $e_{31} = -4.4$, $e_{33} = 18.6$, $e_{15} = 11.6$ C/m^2;
$h_{11} = 1.1151 \times 10^{-8}$, $h_{33} = 1.2567 \times 10^{-8}$ C/(Vm);
$\varepsilon^S_{33} = 4.15 \times 10^{-3}$, $p^S = 0.23$ Cm^{-2}.

For the 2D analysis, we take $\varepsilon^S_{11} = -\varepsilon^S_{33}$, while for the 3D analysis, we use $\varepsilon^S_{11} = \varepsilon^S_{22} = -\varepsilon^S_{33}/2$. This will result in zero net spontaneous strain and polarization in the initial state before applying any loads.

The hardening parameters and the switching threshold values are taken to be:
$H_\varepsilon = 3 \times 10^9$ Pa, $H_P = 10^6$ Vm/C, $k_{90} = 1.42 \times 10^5$ Pa, $k_{180} = 2k_{90}$

The 2D specimen is a square with L = W = 1 mm . The mesh used in the 2D simulation is composed of 200 MVC-RBF elements, equivalent to 402 nodes, each having its own random shape as shown in Fig. 7. The figures also shows the randomly generated direction of the x'_3 -crystallographic axis in each grain.

The lower surface of the specimen is constrained from motion in the X_3 direction, while the left surface is not allowed to move in the X_1 direction. Constraints were used to keep the upper and right surfaces (edges in 2D analysis) straight. The lower surface is earthed, i.e. has electric potential $\varphi = 0$.

The 3D specimen is a cube with L = W = D =1 mm . 100 MVC-RBF-W elements only are composing the mesh which has 572 nodes as shown in Fig. 8. In addition to the boundary conditions considered in the 2D analysis, the back surface of the 3D specimen is prevented from motion in X_2 direction. The right, upper and front surfaces are constrained to be flat surfaces after deformation. Fig. 9 shows a 3D
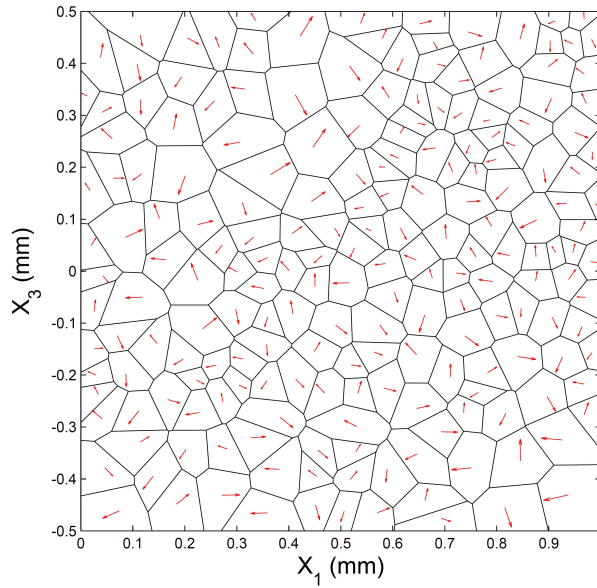
Figure 7: the 2D mesh used in the simulation with the x_3'-crystallographic axis of each grain shown
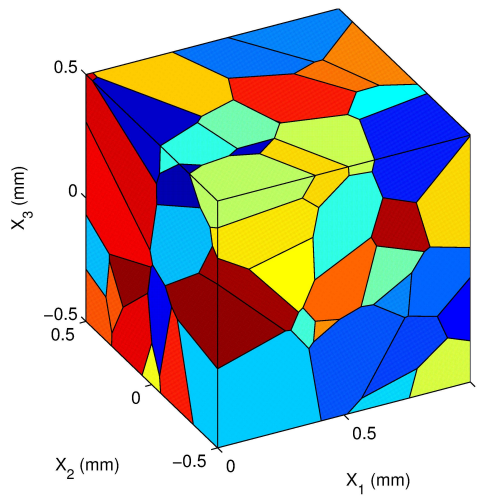

Figure 8: the 3D mesh used in the simulation (100 3D Voronoi cells)

representation of the considered ferroelectric material specimen and all the considered surfaces and dimensions with the global coordinate axes. In 2D analysis we

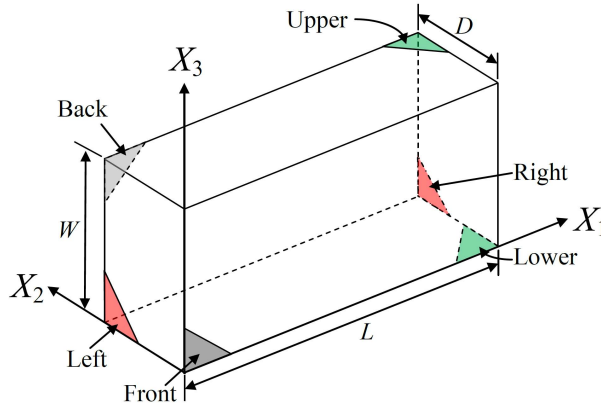only consider the projection of this model on $X_1 - X_3$ plane.

Figure 9: surfaces of the ferroelectric specimen

6.1 Ferroelectric switching

In this case switching is produced by cyclic external electric field applied to the ferroelectric polycrystalline. This results in the hysteresis and butterfly loops of macroscopic electric displacement and strain, respectively, versus electric field. Constant applied external compressive stresses cause these nonlinear loops to become flatter. Cyclic electric field is applied by specifying a constant value for the electric potential on the upper surface while the lower surface is earthed. The value of the electric potential on the upper surface is expressed as:

$$\overline{\varphi}(t) = W \times E \sin(2\pi f t) \tag{82}$$

Where $E = 20 \times 10^5$ V/m is the amplitude of the applied electric field, and $f = 60$ Hz is the frequency of the applied electric load. t is the time in second. The time step used in the simulation is $\Delta t = 1/(624f) = 2.6709 \times 10^{-5}$ sec . In addition, constant compressive stress is applied on the upper surface of the specimen.

The experimentally observed material behavior for PZT-51 under the loading conditions considered is reported in [Li et al. (2006)] and also shown in Fig. 10. Corresponding simulation results, namely representative hysteresis loops of macroscopic electric displacement - electric field and butterfly curves of macroscopic strain - electric field, are shown in Fig. 11 for the 2D model. The simulation results match the experimental investigations, even though a two-dimensional formulation is considered and the material parameters adopted do not fully reflect the local properties

of the material used for the experimental investigations (as these are not directly available in the literature).

The macroscopic electric displacement and strain are the area average electric displacement and strain calculated as:

$$D_3 = \frac{\sum_{k=1}^{N} \int_{A^k} D_3^k(\xi^\gamma) dA}{A} \tag{83}$$

$$\varepsilon_3 = \frac{\sum_{k=1}^{N} \int_{A^k} \varepsilon_3^k(\xi^\gamma) dA}{A} = \frac{\sum_{k=1}^{N} (\bar{\varepsilon}_3^{Lk} + \varepsilon_3^{Rk}) A^k}{A} \tag{84}$$

Where A is the total surface area of the specimen $A = L \times W$. For the 3D analysis, we use the volume average macroscopic strain which is calculated similarly but replacing the area integral by a volume integral in each element and dividing by the total volume of the specimen instead of the total area.
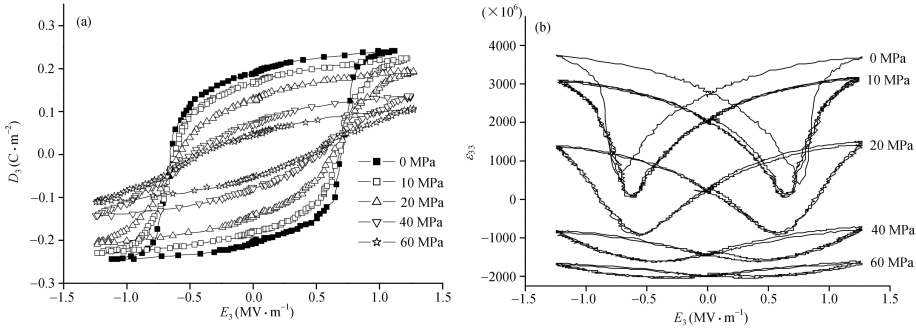
Figure 10: Experimental observation of a ferroelectric polycrystal (PZT-51) under electromechanical loading conditions with a cyclic external electric field and constant external compressive stresses, taken from [Li *et al*. (2006)]: (left) macroscopic electric displacement and (right) macroscopic strain

Both Fig. 10 and Fig. 11 clearly show that increasing the magnitude of the constant uniaxial compressive stresses causes the hysteresis loop to contract. The microscopic or rather physical background for this macroscopically observed behavior lies in the fact that at larger external compressive stresses, domain switching processes locally experience higher resistance for switching. The butterfly curves show similar behavior, except that the curves are also shifted towards the compressive regime for increasing external compression levels. Moreover, the simulated response curves in Fig. 11 are smooth, which is not the case for several FEM-based discrete switching models reported in the literature, but here stems from the incorporation of hardening contributions (back fields).
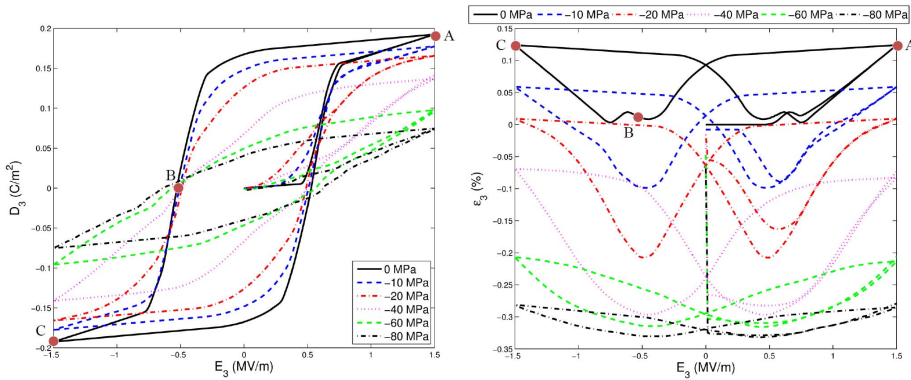
Figure 11: Simulated response of ferroelectric polycrystalline under electromechanical loading conditions with a cyclic external electric field and constant external compressive stresses (2D mesh: 200 MVC-RBF)

For the 3D case, Fig. 12 shows the hysteresis and butterfly loops for different levels of externally applied compressive stresses on the upper surface.
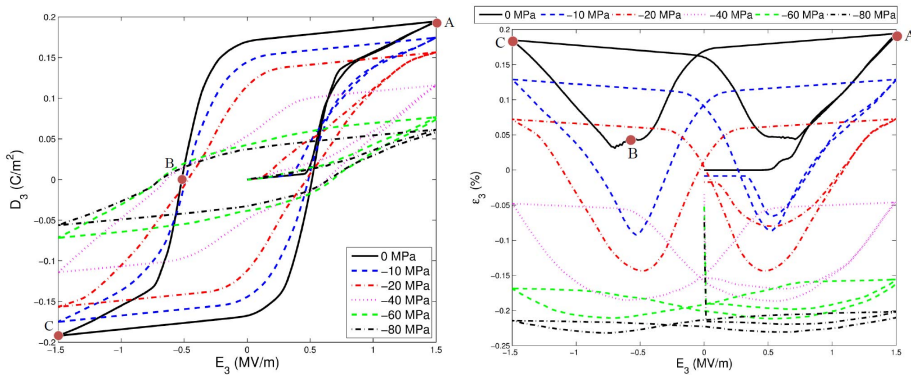

Figure 12: Simulated response of ferroelectric polycrystalline under electromechanical loading conditions with a cyclic external electric field and constant external compressive stresses (3D mesh: 100 MVC-RBF-W)

Even though any regular mesh can also generate the same macroscopic response, the microstructure of the regular mesh will not be similar to that of the physical specimens because of the difference in grain geometries. The macroscopic response is just the average of the local response. So higher and lower values of stress and electric field can exist locally inside the specimen, but on average they

are canceled out. In order to show this, Fig. 13 presents the distribution of the X_3 -component of strain, stress, electric field and electric displacement at three instants during the electric loading cycle in the absence of any applied compressive stress. These 3 particular points referred to as "A", "B" and "C" are shown in the hysteresis and butterfly curves ("A": fully poled along the positive X_3 -axis; "B": electrically depoled; "C": fully poled along the negative X_3 -axis). Fig. 14 shows the same distributions for the 3D model. The plots are slightly transparent to show the distribution of the fields in the internal elements. Moreover, in Fig. 15 some elements are removed from the model to clearly visualize the stress distribution, as an example, in the inner elements. (The model is also rotated in Fig. 15 for better visualization).

The plots of the electric displacement in Fig. 13 at loading points "A" and "C" display that the specimen is almost completely poled with respect to the macroscopic loading direction while at the macroscopically depoled state "B", some individual crystals show zero net contribution to the projected electric displacements. Other crystals, however, still show non-vanishing contributions either in positive or negative direction of the X_3 -axis. This can also be seen in Fig. 14 for the 3D model. On the macroscopic level, however, these contributions in average cancel each other out so that the overall specimen possesses a negligible polarization as graphically displayed in the hysteresis loop in Fig. 11 and Fig. 12. The simulation results not only show the same macroscopic strain level at states "A" and "C", but also similar internal strain field distribution as presented in Fig. 13 for the 2D model. By analogy, similar stress contributions are observed at these two states as well. However for the 3D model in Fig. 14, the strain and stress distribution is not exactly similar at points "A" and "C" because the sequence of switching occurred to reach point "A" is different from the switching sequence that occurred to achieve point "C". Even though the level of macroscopic strain at these two instants may be similar, the local strain distribution is different. The locations of stress concentration are different because the switching sequence is the process that governs the intergranular effects. For the depoled state "B", the strains in most of the individual crystals are close to zero. The local stress distribution along the X_3 -axis turn out to take non-vanishing values within some grains in all the three states "A", "B" and "C" even though their averaged values on the macroscopic scale are negligible. Similarly but not that pronounced, a non-homogeneous distribution of the electric field E_3 is observed.

6.2   *Ferroelastic switching*

A uniformly cyclic stress is applied on the upper surface of the polycrystalline ferroelectric specimen to cause switching. This case of loading causes only 90°
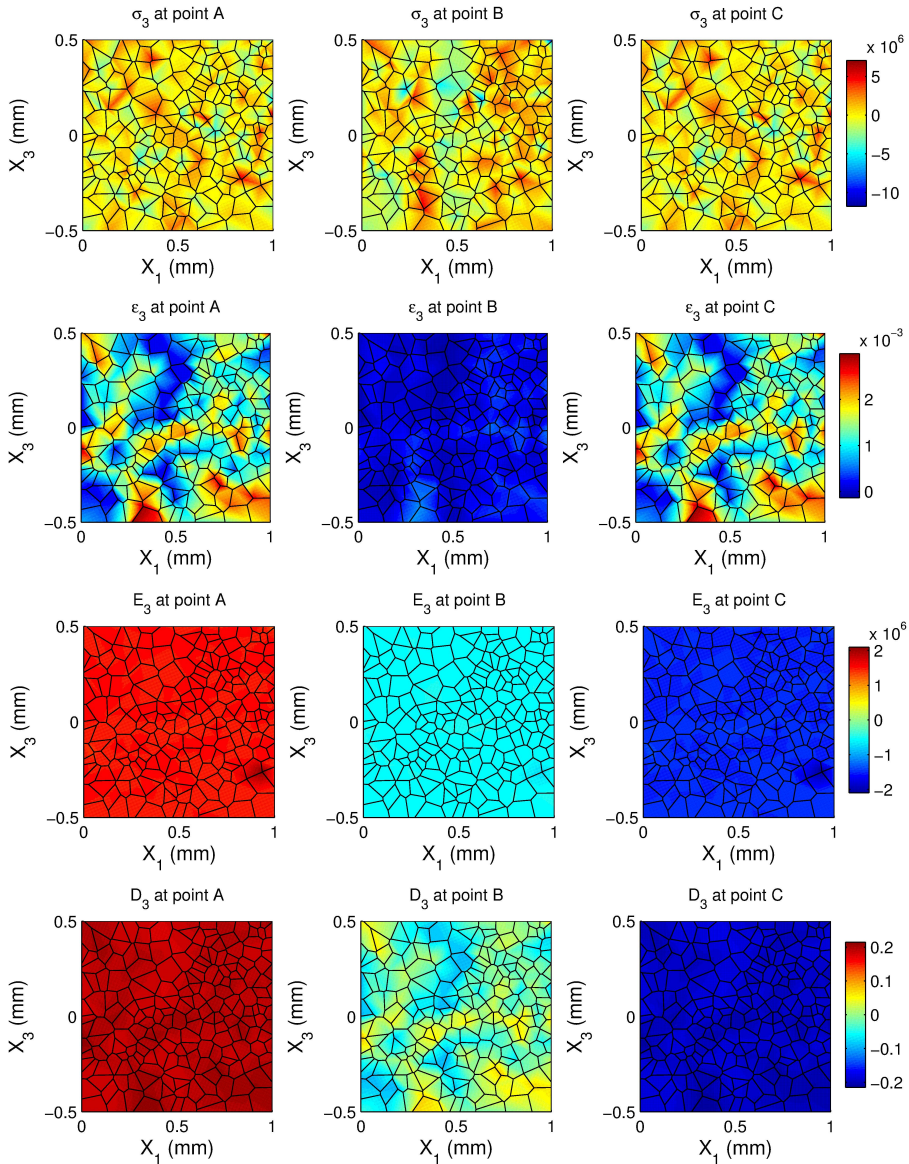
Figure 13: Simulation results representing the local distribution of strain, stress (Pa), electric field (V/m) and electric displacement (C/m^2) at points "A", "B", and "C"
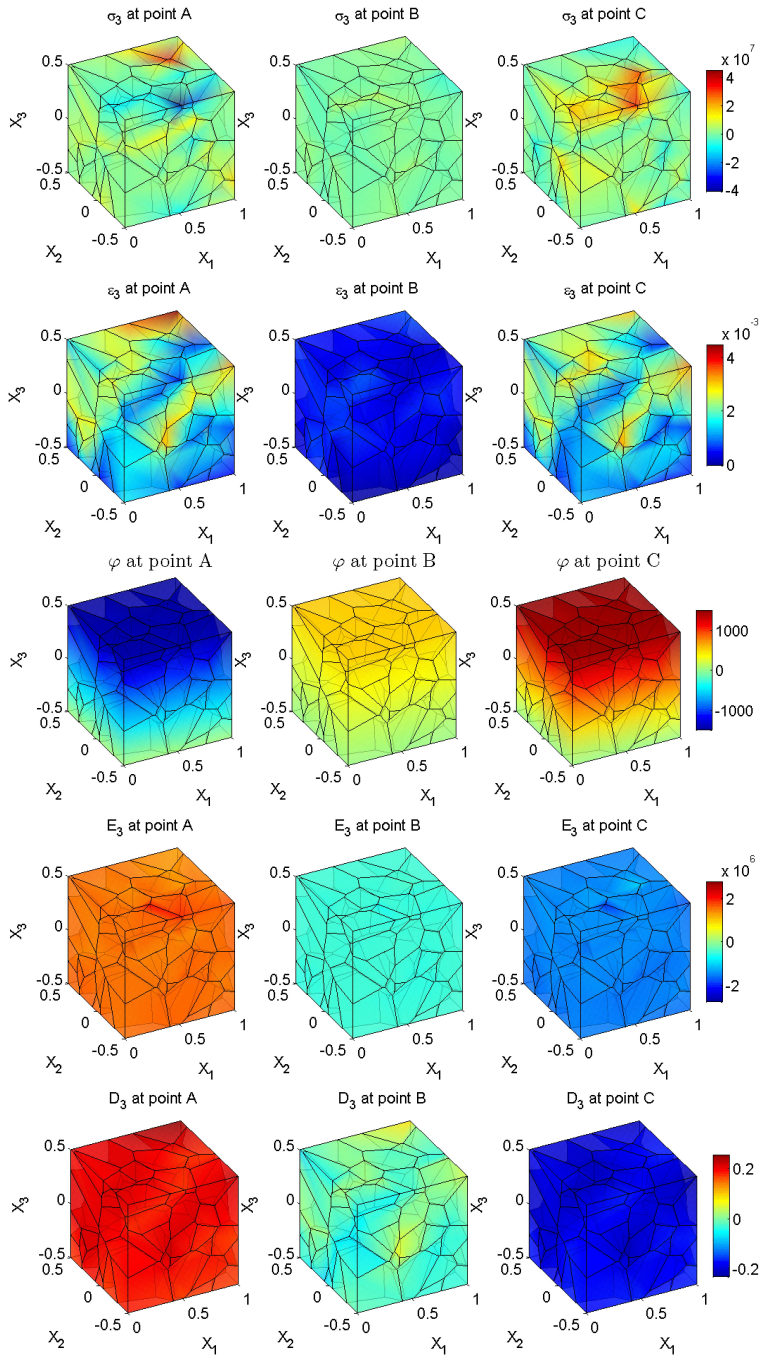
Figure 14: Simulation results representing the local distribution of strain, stress (Pa), electric potential (V), electric field (V/m) and electric displacement (C/m^2) at points "A", "B", and "C" (3D model: 100 MVC-RBF-W elements)
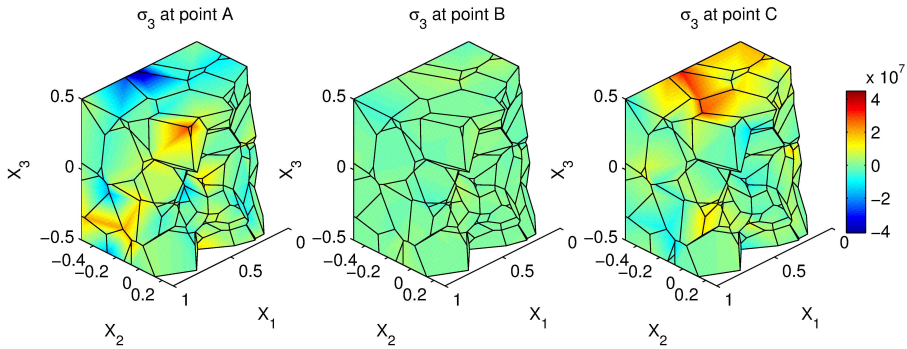
Figure 15: Some elements are removed from the ferroelectric specimen to show the stress distribution (Pa) in the inner elements

switching. Since there is no applied electric field ($\overline{\mathbf{E}} = \mathbf{0}$), then the driving force, f_{ij}, in Eq. 74 is only dependent on the applied stress, $\overline{\mathbf{t}}$, the back stress, $\boldsymbol{\sigma}^{\mathbf{b}}$, and the difference in the domains' spontaneous strain vectors, $\boldsymbol{\varepsilon}^{\mathbf{s}}_{i \to j}$. Hence any 180° switching is prevented in all elements (i.e. $f_{12} = f_{34} = f_{56} = 0$), and we get the same value of volume fraction for types 1 and 2 domains and another value of volume fraction for types 3 and 4 domains (and a third value for domains of types 5 and 6 in 3D analysis) in each element in each simulation step. Consequently, the element piezoelectric matrix ($\mathbf{e}^k$ or $\mathbf{m}^k$), and remnant polarization vector, $\mathbf{P}^{\mathbf{R}k}$, are always zero, and then the element macroscopic electric displacement, $\mathbf{D}$ will also be zero. So ferroelastic is easier than ferroelectric switching because the switching only affects the mechanical variables and the problem is reduced to a pure elastic problem with spontaneous strain that changes every time step as the domains switch in each grain by 90°. For our simulations, the cyclic uniform stress that is applied on the upper surface of the specimen is expressed as:

$$\overline{t}_3(t) = \sigma \sin(2\pi f t) \tag{85}$$

Where $\sigma = 100$ MPa is the amplitude, and $f = 20$ Hz is the frequency of the applied mechanical load; t is the time in second. The time step used in the simulation is $\Delta t = 1/(624f)$. For the 2D model, Fig. 16 (left) shows the hysteresis loop of the applied stress- macroscopic strain, while Fig. 17 shows the hysteresis loop for the 3D model. In each 2D element there are two domain types or variants more aligned to X_3 - axis while the other 2 are more aligned to the X_1 - axis. The switching process change the amount of the X_1 - and X_3- aligned domains or volume fractions in the whole specimen as shown in Fig. 16 (right). The results presented here together with the results of Kim and Jiang (2002) and Sze and Sheng (2005) are in

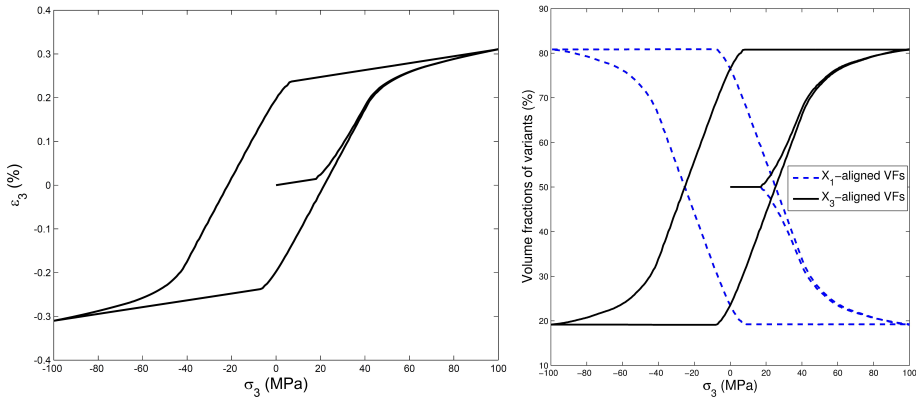qualitative agreement with the experimental observations.

Figure 16: (Left): Stress-strain hysteresis loop in ferroelastic switching, (right): X_1 - and X_3 - aligned volume fractions in ferroelastic switching (2D model)
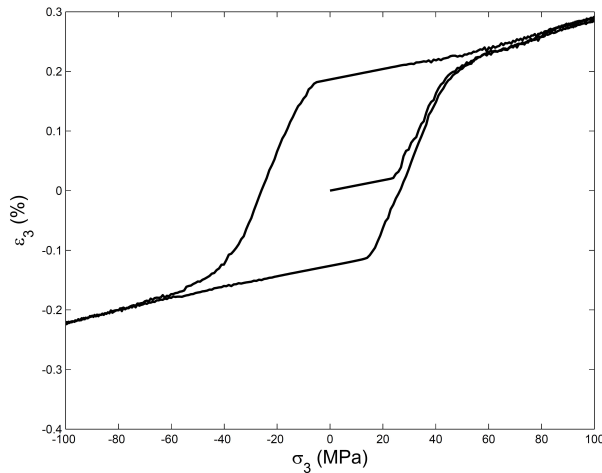

Figure 17: Stress-strain hysteresis loop in ferroelastic switching (3D model)

It should be noted that since the VC mesh is random and also the crystallographic axes in each element or grain is random, as the domain descritization and the random distribution of the crystallographic axes change, the resulting loop is slightly changed.

7   Conclusions

2D as well as 3D models of the Multiphysics Voronoi Cells based on radial basis functions, to describe the primal variables (mechanical displacements and electric potential) in the interior of each finite element as well as linear functions to describe the primal variables on the element boundaries, were developed to simulate ferroelectric and ferroelastic switching in ferroelectric ceramic materials. The linear functions used at the surfaces of the 3D VCs are based on the Washspress functions. The compatibility between the assumed fields in the interior of the element and those on the boundaries is met, using either the collocation or the least squares methods. Independently assumed strain and electric fields can also be used to avoid the shear locking problem. The compatibility between these independently assumed secondary fields and those derived from the primary fields is also met using the same mentioned methods.

The developed 2D and 3D MVCs were able to simulate ferroelectric and ferroelastic switching phenomena accurately, as compared to previous models in the literature and the experimental results. The complexity of geometry and domains orientation of the ferroelectric specimens as well as the distribution of the mechanical and electric fields during the cyclic electromechanical loading can now be fully simulated using the 3D MVCs (MVC-RBF-W), and the randomly generated crystallographic axes in each grain. Each MVC represents a crystal grain having a random shape, and surrounded by a different number of neighboring elements or grains.

This is the first time for 3D Multiphysics Voronoi Cells (MVC) to be implemented in a ferroelectric switching model. It was shown here that during the cyclic loading, domain switching can cause localized stresses inside the specimen and this is one of the causes of crack nucleation in ferroelectric materials. These localized stresses are not apparent in the macroscopic response which gives average values of the field distributions. However, the internal distributions are visualized here to show the localized concentrations of stresses and strains. In this work it was observed with the 3D model that points with similar macroscopic stresses and strains may have different stress and strain distributions. The cause of this is thought to lie in the fact that the sequence of switching is different as the body is being loaded to the points having the same level of macroscopic strain. The difference in this switching sequence causes the locations of the concentrated stresses and strains to change. Experimental testing is needed to verify this observation.

References

Arockiarajan, A.; Delibas, B.; Menzel, A.; Seemann, W. (2006): Studies on rate-dependent switching effects of piezoelectric materials using a finite element model. *Comput Mater Sci*, vol. 37, pp. 306-317.

Arockiarajan, A.; Menzel, A.; Delibas, B.; Seemann, W. (2007): Micromechanical modeling of switching effects in piezoelectric materials- a robust coupled finite element approach. *J Intell Mater Syst Struct*, vol. 18, pp. 983-999.

Atluri, S.N. (2005): *Methods of Computer Modeling in Engineering & Sciences, Volume I*, 540 pages, Tech Science Press, USA.

Babuska, I. (1973): The finite element method with Lagrangian multipliers. *Numerische Mathematik*, vol. 20, no. 3, pp. 179-192.

Bishay, P. L.; Atluri, S. N. (2012): High-Performance 3D Hybrid/Mixed, and Simple 3D Voronoi Cell Finite Elements, for Macro- & Micro-mechanical Modeling of Solids, Without Using Multi-field Variational Principles, *CMES: Computer Modeling in Engineering & Sciences*, vol. 84, no. 1, pp. 41-98.

Brezzi, F. (1974): On the existence, uniqueness and approximation of saddle-point problems arising from Lagrangian multipliers. *Revue Francaise D'automatique, Informatique, Recherche Opérationnelle, Analyse Numérique*, vol. 8, no. 2, pp. 129-151.

Cocks, A.C.F; McMeeking, R.M. (1999): A phenomenological constitutive law for the behavior of ferroelectric ceramics. *Ferroelectrics*, vol. 228, pp. 219-228.

Dong, L.; Atluri, S. N. (2011): A simple procedure to develop efficient & stable hybrid/mixed elements, and Voronoi cell finite elements for macro- & micromechanics. *CMC: Computers, Materials & Continua*, vol. 24, no. 1, pp. 61-104.

Dong, L.; Atluri, S. N. (2012 a): A Simple Multi-Source-Point Trefftz Method for

Solving Direct/Inverse SHM Problems of Plane Elasticity in Arbitrary Multiply-Connected Domains. *CMES: Computer Modeling in Engineering & Sciences*, vol. 85, no. 1, pp. 1-43.

Dong, L.; Atluri, S. N. (2012 b): T-Trefftz Voronoi Cell Finite Elements with Elastic/Rigid Inclusions or Voids for Micromechanical Analysis of Composite and Porous Materials. *CMES: Computer Modeling in Engineering & Sciences*, vol. 83, no. 2, pp.183-219.

Dong, L.; Atluri, S. N. (2012 c): Development of 3D T-Trefftz Voronoi Cell Finite Elements with/without Spherical Voids & /or Elastic/Rigid Inclusions for Microme-chanical Modeling of Heterogeneous Materials. *CMC: Computers, Materials & Continua*, vol. 29, no. 2, pp. 169-211.

Dong, L.; Atluri, S. N. (2012 d): Development of 3D Trefftz Voronoi Cells with Ellipsoidal Voids & /or Elastic/Rigid Inclusions for Micromechanical Modeling of Heterogeneous Materials. *CMC: Computers, Materials & Continua*, vol. 30, no. 1, pp. 39-82.

Ghandi, K., Hagwood, N.W. (1996): Nonlinear finite element modeling of phase transitions in electro-mechanically coupled material. *SPIE Proc.*, vol. 2715, pp. 121-139.

Ghosh, S. (2011): *Micromechanical Analysis and Multi-Scale Modeling Using the Voronoi Cell Finite Element Method*. CRC Press/Taylor & Francis.

Haug, A.; Huber, J.E.; Onck, P. R.; Van derGiessen, E. (2007): Multi-grain analysis versus self-consistent estimates of ferroelectric polycrystals. *J Mech Phys Solids*, vol. 55, pp. 648-665.

Huo, Y., Jiang, Q.(1997): Modeling of domain switching in polycrystalline ferro-electric ceramics. *J. Smart Mat. Struct.*, vol. 6, pp. 441-447.

Huo, Y., Jiang, Q. (1998): Modeling of domain switching in ferroelectric ceram-ics: an example. *Int. J. Solids Struct.*, vol. 35, pp. 1339-1353.

Hwang, S.C., McMeeking, R.M. (1998): A finite element model of ferroelectric polycrystals. *Ferroelectrics*, vol. 211, pp. 177-194.

Hwang, S.C., McMeeking, R.M. (1999): A finite element model of ferroelastic polycrystals. *Int. J. Solids Struct.*, vol. 36, pp. 1541-1556.

Jayabal, K.; Menzel, A.; Arockiarajan, A.; Srinivasan, S. M. (2011) Micromechanical modeling of switching phenomena in polycrystalline piezoceramics: application of a polygonal finite element approach. *Comput Mech*, vol. 48, pp. 421-435.

Kamlah, M.; Jiang, Q. (1999): A constitutive model for ferroelectric PZT ceramics under uniaxial loading. *Smart Mater Struct*, vol. 8, pp. 441- 459.

Kamlah, M.; Liskowsky, A.C.; McMeeking, R.M.; Balke, H. (2005): Finite element simulation of a polycrystalline ferroelectric based on a multi-domain single crystal switching model. *Int. J. Solids Struct.*, vol. 42, pp. 2949-2964.

Kim, S.J.; Jiang, Q. (2002): A finite element model for rate-dependent behavior of ferroelectric ceramics. *Int J Solids Struct*, vol. 39, pp. 1015- 1030.

Kim, S. J.; Choi, J.; Kwak, M.K. (2003): A finite element prediction of ferroelectric switching behavior using a regular dodecahedron RVE. *Computational Mechanics*, vol. 31, pp. 469-478.

Li, F.; Fang, D.; Lee, J.; Kim, C.H. (2006): Effects of compressive stress on the nonlinear electromechanical behavior of ferroelectric ceramics. *Sci China: Ser E Technol Sci*, vol.49, pp.29-37.

Menzel, A.; Arockiarajan, A.; Sivakumar, S.M. (2008): Two models to simulate rate-dependent domain switching effects- application to ferroelastic polycrystalline ceramics. *Smart Mater Struct*, vol.17, pp. 015026-015038.

Pathak, A.; McMeeking, R. M. (2008): Three-dimensional finite element simulations of ferroelectric polycrystals under electrical and mechanical loading. *J Mech Phys Solids*, vol. 56, pp. 663-683.

Pian, T.H.H. (1964): Derivation of element stiffness matrices by assumed stress distribution. *Am. Inst. Aeronaut. Astronaut.*, vol. J.2, pp. 1333-1336.

Steinkopff, T. (1999): Finite-element modelling of ferroelectric domain switching in piezoelectric ceramics. *J Eur Ceram Soc*, vol. 19, pp. 1247-1249.

Sze, K.Y.; Pan, Y.S. (1999): Hybrid finite element models for piezoelectric materials. *J. Sound Vib.*, vol. 226, pp. 519-547.

Sze, K. Y.; Sheng, N. (2005) Polygonal finite element method for nonlinear constitutive modeling of polycrystalline ferroelectrics. *Finite Elem Anal Des*, vol. 42, pp. 107-129.

Wachspress, E. L. (1975): *A Rational Finite Element Basis, Mathematics in Science and Engineering*. vol. 114, Academic Press.

Webber K.G. (2008): *Effect of Domain Wall Motion and Phase Transformations on Nonlinear Hysteretic Constitutive Behavior in Ferroelectric Materials*. PhD dissertation, Georgia institute of technology.